Ice Nucleation Activities of Carbon-Bearing Materials in Deposition Mode: From Graphite to Airplane Soot Surrogates

Raouf Ikhenazene, Claire Pirim, Jennifer A. Noble, Cornelia Irimiea, Yvain Carpentier, Ismael Ortega, François-Xavier Ouf, Cristian Focsa, Bertrand Chazallon

TITLE

Ice Nucleation Activities of Carbon-bearing Materials in Deposition Mode: from Graphite to Airplane Soot Surrogates

AUTHOR NAMES

Raouf Ikhenazene,[1] Claire Pirim,[1] Jennifer A. Noble,[1†] Cornelia Irimiea,[1‡] Yvain Carpentier [1] Ismael K. Ortega,[1‡] François-Xavier Ouf,[2] Cristian Focsa,[1] and Bertrand Chazallon[1]*

AUTHOR ADDRESS

[1]Univ. Lille, CNRS, UMR 8523 – PhLAM – Physique des Lasers Atomes et Molécules, CERLA – Centres d'Etudes et de Recherches Lasers et Applications, F-59000 Lille, France.

[2] Institut de Radioprotection et de Sûreté Nucléaire (IRSN), PSN-RES, SCA, LPMA, Gif-sur-Yvette, 91192, France.

ABSTRACT

Soot particles emitted by aircraft engines may act as ice nuclei (IN) within the atmosphere, subsequently triggering the formation of condensation trails. Such contrails might further evolve as cirrus clouds, and thus greatly influence the Earth's radiative budget and impact the amount of precipitation. In order to monitor in-situ deliquescence, efflorescence, and nucleation processes followed by ice growth in the laboratory, we developed the Ice and Droplet Nucleation Experimental Setup (IDroNES), which combines optical imaging and micro-Raman measurements to follow nucleation events in a pressure-, temperature- and humidity-controlled optical chamber. We first compare against literature data, and later confirm, the deliquescence relative humidities of micron-sized sodium chloride salt crystals in the -5°C to -35°C temperature range. Then, we investigate the ice nucleation activity of graphite and aircraft soot analogs, in the -15°C to -45°C temperature range, when exposed to humid nitrogen (N_2/H_2O gas flow). Soot samples exhibiting various surface chemistries, morphologies, and sizes are thoroughly examined via mass spectrometry, and spectroscopic and optical techniques. All carbon-bearing samples are found active at nucleating ice at low ice saturation ratios (S_{ice} determined when the first crystal is detected). When normalizing S_{ice} to the total surface area of a sample, one can derive the ice-active surface site density (n_s). This parameter provides a means to compare the ice nucleating behavior of various particle types with distinct surface areas. As all samples studied in our work feature large surface areas, we provide ice nucleation data (S_{ice} and n_s) for a range of surface areas that remained largely unexplored to date. We find that the interplay between surface composition and morphology (micro, meso, and macro pores, surface roughness) influences the ice onset relative humidity.

INTRODUCTION

Aircraft engines emit hot gases (carbon dioxide, nitrogen oxides, sulfur oxides, and water vapor) and aerosol particles (including soot particles) that can affect the atmospheric chemical composition from the upper troposphere to the lower stratosphere between 9 and 12 km[1] and impact local air quality at ground-level in the vicinity of airports.[2] In fact, with global traffic topping 7.7 billion passengers in 2016, and expected to double by 2031,[3] aviation's impacts on climate and health are great sources of concern within the scientific community and among policy makers.

Measurements of soot emissions resulting from incomplete combustion of fuel during the APEX campaigns were shown to reach 10^{15}-10^{17} particles per kilogram of burned fuel,[4] which are comparable to the number of particles generated from ship emissions, biomass burning and forest fires[2] (on a per unit fuel burn basis). Once emitted by aircraft engines, these 5-100 nm spherical aerosols[2, 5-6] can further coagulate within the exhaust plume and form complex fractal-like agglomerates causing a second mode of larger particles (100-500 nm) to exist.[7-9] Depending upon the connectivity between the primary particles, these aggregates exhibit a compact or lacy character, forming either near point contacts between individual particles or conversely, merging and fusing primary particles together.[10] Soot particles of the size range 0.01-1.9 μm have been measured by the Advanced Technology Research Aircraft in a soot-rich contrail with concentration peaks reaching over 4000 particles per cubic centimeter.[11] Consequently, relatively high concentrations of large soot particles may be transitory present in the atmosphere at airliners' cruising altitudes.

In the atmosphere, aerosol particles may act as cloud condensation nuclei (CCN) or ice nucleating particles (INPs) and subsequently trigger the formation of condensation trails. These contrails may evolve into aerosol-induced cirrus clouds, as long as the ambient air is supersaturated with respect to ice.[12] Contrail cirrus clouds are dominated by high concentrations (100 cm^{-3}) of ice crystals with mean diameters in the range 1–10 μm, whereas ice crystals in the range 10–20 μm diameter with concentrations of 2–5 cm^{-3} have been observed in young cirrus clouds.[13] When humidity, pressure, and temperature conditions are met for the background air to be supersaturated with respect to ice, soot particles can thus serve as cold surfaces onto which nucleation of ice can occur and greatly influence the Earth's energy budget,[12-14] change the ice crystal number concentration[15] or crystal size, and hence impact the hydrological cycle. Aircraft linear contrails are estimated to cover 0.06-0.15% of the Earth's surface on an annually averaged basis[16-18] and aircraft-induced cirrus clouds have a potential global coverage of about 15%.[19-20] The main path to contrail formation is the activation, growth, and subsequent freezing of supercooled water droplets within the aircraft's exhaust plume, where the relative humidities usually reach values above water saturation. Nevertheless, some contrail ice particles might form from vapor deposition upon suitable nuclei, provided the plume is ice supersaturated during mixing with ambient air.[21]

Most of the laboratory studies assessing the ability of carbonaceous particles to nucleate ice have used carbon standards or laboratory surrogates to simulate aircraft soot particles. Because unprocessed aircraft particles may be difficult and expensive to come by, numerous studies have rather turned to laboratory flame burners or soot generators to produce soot particles which only partly simulate aircraft soot, but for which different chemistries or structural parameters can be generated (e.g. aviation kerosene flame soot, acetylene soot, lamp black, n-hexane soot, kerosene burner exhaust soot, graphite spark, furnace black, Combustion Aerosol Standard generator soot,

Palas soot, etc.)[23].[22] However, detailed analyses of the particles' surface chemical composition and structural properties (pore size, effective surface area) often lack and the particles' behavior regarding ice nucleation may be interpreted as a generic behavior for "typical" carbon-bearing samples, thereby discarding any chemical or structural specificity the sample may have. Most ice nucleation studies have been performed in immersion mode, and generally classified carbon-containing particles as non-active,[23-27] i.e. necessitating relative humidity ratios (RH) above water saturation to trigger ice nucleation. A few experimental studies rather focused on the alternative formation path, i.e. by vapor deposition, and ended up not being as conclusive, founding soot particles either active[28-35] (i.e. nucleation observed at RH above ice saturation but below water saturation) or non-active.[28-31, 36] Owing to the complex nature of these materials, with great chemical and morphological variabilities depending upon their origin, widespread results as to their ice nucleation abilities for the same nucleation mode (deposition) are found in the literature. Discrepancies in ice nucleation results can arise from various sources. First, from the detection threshold - often inherent to the technique used to probe nucleation events. For instance, a sample can be defined as active from its ice nucleation onset, i.e. the first crystal detected, or from its activated fraction, commonly found between 0.001% and 10% in the literature,[37] provided they are obtained in temperature-RH conditions representative of the heterogeneous nucleation regime. Therefore, a sample can be observed as being active from its ice nucleation onset, yet exhibiting only a few ice crystals over the whole aerosol population and over the time of the experiment. Alternative measurements[38-39] include the amount of adsorbed water (in terms of monolayers) at a given RH. In addition, ice nucleation abilities were shown to depend upon temperature regimes, where black carbon samples were found non-active in mixed-phase clouds (MPCs) regimes (above -38°C) but potentially active in cirrus clouds (CCs) regimes[40] (below -38°C). The work by Mahrt

and coworkers[40] showed how particle size and the presence of mesopores (2-50 nm) can stimulate ice nucleation activity on soot samples in CCs temperature regimes. This also illustrates how variabilities in carbon-bearing particles' physicochemical properties likely contribute to widespread ice nucleation activities results. Parameters influencing ice nucleation activities can include distinct surface chemical compositions (presence of coatings, [30, 33, 41-44] nature of organics, oxidation,[45-46] hygroscopicity,[27, 32] surface morphologies (shape, pore size or particle sizes[40]), aggregate size or effective surface area) - even when originating from the same combustion source. Umo and coworkers[47] also shown that the ice-active fraction of some coal fly ash samples would increase, and trigger ice nucleation activity at a very low RH ratio with respect to ice (101-105%), when the particles first undergo a cooling cycle producing ice germs that remain in the pores during warming and induce ice crystallization as soon as the pre-activated particles experience ice-supersaturated conditions at warmer temperatures. It is hence not only the particle itself but also its temperature and humidity history that condition its activity. Efforts to untangle individual contributions of the aforementioned parameters in triggering ice nucleation activities on carbon-bearing particles are still in progress and more nucleation studies can provide new approaches to help understanding such complex phenomena.

In this context, we developed a new instrument, the so-called Ice and Droplet Nucleation Experimental Setup (IDroNES), which is a combination of a micro-Raman instrument and a temperature, pressure and humidity-controlled chamber that allows for both optical and spectroscopic monitoring of nucleation and deliquescence/efflorescence processes. Due to its optical capabilities, IDroNES can also yield information on crystal habits formed during nucleation and permit the differentiation of supercooled droplets from ice nuclei (IN) when applicable. As a proof of concept, IDroNES is first validated using sodium chloride salt for which deliquescence

relative humidities (DRH) with respect to the temperature are well established in the literature[48-50] and then utilized to study the ice nucleation activity of silicon, graphite, and laboratory soot samples that can mimic some of the properties of aircraft soot surrogates.[51] Then, the ice nucleation activity is investigated on various types of samples in conjunction with thorough chemical surface analyses and an optical surface topography method (for selected data). We report the ice nucleation activity of silicon, graphite, and kerosene and miniature Combustion Aerosol Standard generator (miniCAST) soot, covering a temperature range between -15°C and -45°C and exposed to humid nitrogen. The aim is to expand our understanding of ice nucleation on well-characterized soot particles of varying organic content, morphologies, and specific surface areas (from individual particles to a film) using the same experimental scheme.

EXPERIMENTAL METHODS

Sample preparation. The nucleation activities of a variety of carbon-bearing samples with increasing molecular complexity and structural variability have been studied. Samples consist of graphite flakes (100 mesh, Sigma Aldrich) and airplane soot surrogates originating from two different burners. Soot samples were either produced using a modified McKenna burner supplied with kerosene Jet A1 fuel or a mini Combustion Aerosol STandard generator (miniCAST Jing Ltd, 5201C), which produces soot particles within a fuel gas/oxidant gas co-flow diffusion flame. Briefly, soot particles originate from the combustion of the oxidizer (air) with the combustible (propane, C_3H_8) by diffusion. Particles are subsequently extracted from the flame by a perpendicular stream of quenching gas (N_2) to first, prevent further physico-chemical processes to occur in the particle stream, and second, stabilize soot particles in such a way that condensation in the particle stream is inhibited. Further dilution gas (compressed air) is added to the quenching gas to ensure proper dilution of the particle stream. The nature and flow rates of the gases involved in

soot production and extraction (oxidizer, fuel, quench gas, dilution gas) govern the overall flame richness, soot morphology, surface composition, and hence the soot particles' optical and chemical properties. Both graphite and soot samples were collected on optically polished 185 µm-thick silicon wafers of 22 mm diameter (Pi-Kem, Ltd) that were chosen for their good heat resistance during soot collection, their relatively good thermal conductivity between -55°C and -15°C, and their little to no effect on ice nucleation in immersion mode.[52] Two kerosene soot samples were collected from an atmospheric diffusion flame, at different heights above the McKenna burner, i.e. at 3 cm (Kero-03) and 14 cm (Kero-14). Two CAST set points (SP) were investigated, and are referred to hereafter as CAST-3 and CAST-1. Table S1 presents the miniCAST burner experimental conditions for generating CAST-3 and CAST-1 soot samples. Further information regarding their production can be found in other articles.[53-54] CAST samples with different soot coverages on the silicon wafer were produced by increasing collection time from 5 minutes (CAST-3 and CAST-1) to 20 minutes (CAST-3b and CAST-1b). Sample CAST-3c was first collected onto a quartz filter (Whatman QM-A), subsequently scraped off the filter surface in order to collect free powder, and finally deposited onto the same type of silicon wafer that was used for the other samples. All samples were stored in a dark, dry, and cold environment after production before their nucleation activity was investigated, and were not preheated before being processed.

Description of IDroNES. The Ice and Droplet Nucleation Experimental Setup (IDroNES) newly implemented and presented for the first time in this work is schematically depicted in **Figure 1**. It has been designed for nucleation experiments in deposition mode, i.e. directly by water vapor deposition. The setup includes a humidity control system that produces a constant H_2O/N_2 flow at constant pressure and at room temperature. The N_2 gas flow (Air Liquide, 99.9998% purity) is pressurized to 2 bar and subsequently separated into two gas inlets. One gas stream passes through

a first flow meter (El-Flow, Bronkhorst), and is further passed through ultra-pure water (Purelab Option-Q) to humidify the gas stream through bubbling. The other N_2 stream passes through a second mass flow controller (Brooks) and both gas flows are recombined downstream in a glass-mixing vessel. The humidity-controlled gas mixture in the vessel is then supplied to the chamber. The chamber is a modified Linkam stage (Scientific Instruments) priorly evacuated to 40 mbar using a 8.3 L/min diaphragm vacuum pump (Ilmvac GmbH). The stage has been designed with many entry ports that enable gas intake and backfilling from different positions relative to the sample stage. The temperature of the sample mount's thermal exchanger is regulated in such a way that the resistive heating and the cooling provided by liquid nitrogen are precisely balanced. The resulting temperature is then monitored using a PT100 resistance thermometer. The cylindrical thermal exchanger and stainless steel inlets in the chamber are all heat-insulated so that the exchanger's nickel top surface is the only cold point in the cell. The heat exchanger's temperature set point is defined at the beginning of the experiment and remains constant throughout. The experiment starts when the temperature set point is reached and the humidity content in the experimental chamber is very low (with a mixing ratio per volume ranging from 20-1700 ppmv depending on the starting temperature). Then, the nitrogen gas flow rate passing through the water gas bubbler is gradually increased, which subsequently raises the humidity content delivered to the chamber. The system is allowed to equilibrate for a few minutes after each humidity increment. The relative humidity within the chamber is then measured using a cryo-hygrometer (CR-1A, Buck Research Instruments) that indicates the frost point (FP), i.e. the temperature at which the gas mixture is saturated with respect to water vapor over an ice surface with a precision of ± 0.15°C. The dry pump is kept running during the experiment, ensuring a constant flow from the chamber to the cryo-hygrometer, allowing for reactive and accurate humidity readings every 1.8 seconds

between 200-400 mbar. In addition, the chamber possesses an optical window that allows optical and spectroscopic monitoring of the sample surface as the humidity rises. The onset for nucleation is detected using an optical free-space microscope (BXFM Olympus, with 5x, 20x, and 50x magnification objectives) when monitoring the surface at each humidity increment. It is defined here as the ice saturation ratio at which the first ice crystal is observed at the sample surface. The best experimental optical resolution can be inferred from our optical images and sets the detection threshold to about 1.8 µm (with the 50x magnification objective) depending upon the overall image contrast ratio. The best optical detection of ice crystals in our chamber is the result of a trade-off between the greatest optical resolution and the biggest field of view, which often imply the use of several interchangeable magnification objectives (5x, 20x, and 50x). The presence of ice crystals is further confirmed using a Raman spectrometer (InVia Reflex, Renishaw) with a 514.5 nm excitation wavelength (DPSS laser, Cobolt) coupled to the microscope. Specific Raman vibration signatures for hydroxyls (O-H stretches) can pinpoint the nature of the embryo (water versus ice). Spectral acquisition is performed through an Olympus 50× objective (0.5 N.A.) with a laser power typically adjusted to 127 µW at sample (5411 $W.cm^{-2}$) to avoid sample alteration. At the end of the experiment, great care is taken to sublimate rather than melt ice crystals in order to limit sample surface disruption that could occur due to the surface tension of the liquid droplets that will tend to reorganize the uppermost soot particles into islands. To do so, the nitrogen flow passing through the nucleation cell is first dried out to reach a very low RH that triggers crystal sublimation. Only then, sample temperature is increased up to room temperature with a rate of 5 K/min. Following the same rationale, nucleation experiments performed at temperatures above -38°C were done last, as they can modify the sample's topography if water vapor nucleates into droplets.

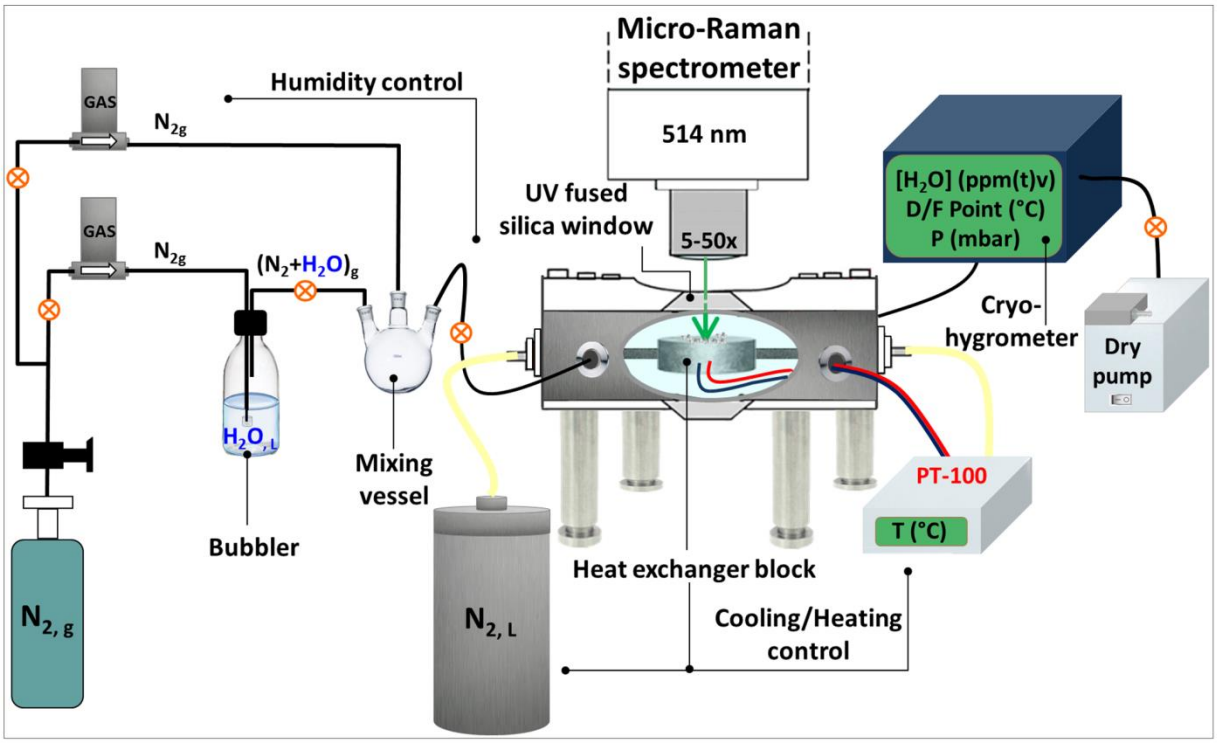

183

184 **Figure 1.** IDroNES: Ice and Droplets Nucleation Experimental Setup. The humidity control
185 system is represented on the left-hand side, the temperature-controlled chamber which contains
186 the heat exchanger block onto which the sample is deposited is shown at the center, and the
187 cryohygrometer giving water concentrations and dew/frost points readings is depicted on the right-
188 hand side of the schematics.

189

190 **Ice saturation ratio (S_{ice}) determination**. The ice saturation ratio (S_{ice}) at which the onset for
191 nucleation is optically observed is calculated using variations on the water vapor pressure
192 formulations developed by Buck (1981). S_{ice} (1) is defined as the ratio of partial water vapor
193 pressure at the nucleation onset temperature (e) to the water saturation vapor pressure over ice at
194 the calibrated sample temperature ($e_{sat,i}$); the water vapor pressure (e) is derived from the cryo-
195 hygrometer (see SI for details):

196 $$S_{\text{ice}} = \frac{e}{e_{\text{sat,i}}} \quad (1)$$

197 The smaller S_{ice}, i.e. the lower the amount of water vapor needed to initiate ice growth on the
198 sample surface, the more active the sample. The contribution to the total error on S_{ice} from the
199 errors on the FP (±0.15°C) and T_{sample} (±2%) are determined using the calculus-based
200 approximation for independent multi-variable functions by adding the components from each
201 variable in quadrature. Thus, the total error on S_{ice} reaches a maximum of about 4%. The nucleation
202 activity of the silicon wafer substrate was tested as a reference to which carbonaceous materials
203 will be compared. Nucleation experiments on silicon wafers were repeated a maximum of five
204 times for each temperature and, accordingly, the resulting S_{ice} is averaged over the repetitions.

205 **Chemical surface analyses.** Soot samples surface chemical composition was probed by two
206 mass spectrometry techniques: Two-step Laser Mass Spectrometry (L2MS) and Secondary Ion
207 Mass Spectrometry (SIMS).[55-56] The custom-built L2MS apparatus has been described in detail
208 elsewhere.[57-60] Briefly, the collimated (2 mm diameter) beam of a Nd:YAG laser (Continuum
209 Minilite II, 5 ns, 532 nm, 10 Hz) irradiates the surface of the sample, placed under vacuum (10^{-8}
210 mbar) on a cryogenic stage. Neutral species in the desorption plume are then ionized by an
211 orthogonal delayed UV beam coming from either a Nd:YAG laser (Continuum Powerlite 8010, 6
212 ns, 266 nm, 10 Hz) for the Resonant Two-Photon Ionization (R2PI) of most of the aromatic
213 species,[61] or a 118 nm (10.5 eV) home-built coherent source[62] in order to enable the Single Photon
214 Ionization (SPI) of most of the condensable species, including aliphatic compounds.[63] Desorption
215 and ionization laser intensities are below, yet close to the fragmentation threshold to optimize the
216 balance between analyte collection and fragmentation. Mass peaks were assigned based on the
217 ionization scheme selectivity and previous results obtained for known standards.[64-65] SIMS

218 analyses were performed using a commercial Time-of-Flight instrument ('TOF.SIMS^5', ION-TOF
219 GmbH). The sample surface was probed in static SIMS mode, where a low dose of primary ions
220 is used to limit molecule fragmentation. A Bi^{3+} 1 ns-pulsed ion beam was accelerated at 25 keV
221 and secondary positive or negative ions were detected by TOF-MS. The primary ion source
222 delivered a pulsed current of 0.3 pA rastered in 25 scans over a 500 × 500 μm^2 area for an
223 acquisition time of 180 s.

224 **Estimation of sample surface area by optical image analysis.** A direct evaluation of CAST (3
225 and 1) soot samples' surface areas was not possible due to the small amount of sample collected
226 at each set point and a limited number of samples. In an attempt to circumvent these obstacles, we
227 developed a new optical analysis method using our micro-Raman spectrometer. The method
228 consists of converting our two-dimensional greyscale optical images into three-dimensional
229 surfaces, revealing the spatial distribution and thickness of our CAST-3 and CAST-1 samples
230 (additional information in the SI).

231 Images of CAST soot samples were taken using the camera on the optical microscope coupled
232 to the Raman spectrometer. Eleven images (at a magnification of 20x) were taken for each soot
233 sample: one image at the center of the sample (central pixel: X_0,Y_0) and five each at 1500 micron
234 intervals along two straight lines radiating from the sample center at 90° from one another (central
235 pixels: X_0,Y_{1500n}, n=1:5, and central pixels: X_{1500n},Y_0, n=1:5). The optical analysis method was
236 developed to determine the spatial distribution and thickness of CAST soot samples deposited on
237 silicon substrates, based upon images such as those presented in the upper panels of **Figure 2**,
238 showing depositions of CAST-1-type and CAST-3-type soot, respectively. The analysis was
239 performed using an in-house MATLAB routine (MATLAB R2014a, The MathWorks, Inc.,
240 Natick, Massachusetts, United States).

A series of calibration measurements were made with the optical microscope on the Raman spectrometer in order to convert greyscale color index (0 to 255) to soot height (in microns) for a CAST-1 soot sample. For each calibration measurement, at a given position (X_i,Y_i) on the sample the microscope was focused first at the silicon substrate surface (i.e. the soot-substrate interface) and secondly at the surface of the deposited soot (i.e. the soot-air interface). In this way, the height of the soot (Z_i) was determined, and the color of the pixel (X_i,Y_i) related to this height was noted.

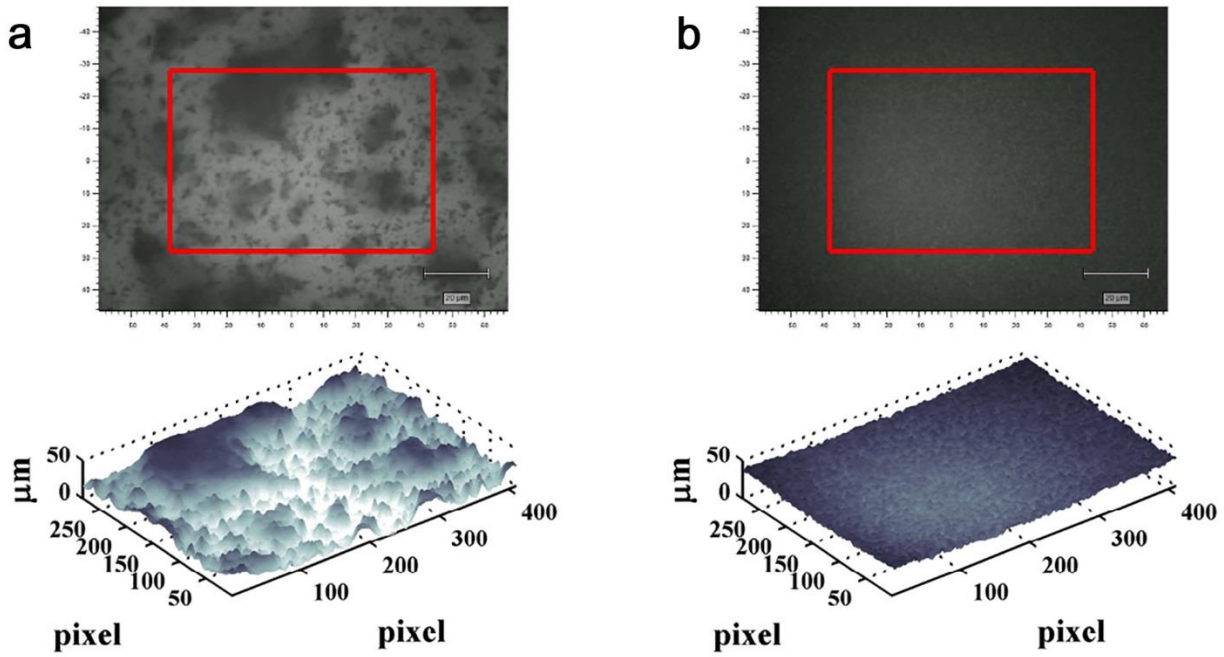

Figure 2. Soot sample data analysis of a) CAST-1, and b) CAST-3. Upper panels: optical microscope images of the center (X_0, Y_0) of the soot samples. The red boxes highlight the area upon which the image analysis was performed and the scale bars represent 20 µm. Lower panels: the three-dimensional surface representations calculated from the optical images of the soot samples.

The relationship between pixel color and height was determined by fitting a straight line to these data. The central 50 x 80 μm^2 area of each greyscale image (red rectangle, **Figure 2**) was thus converted to a three dimensional surface, as illustrated in the lower panels of **Figure 2**. Optical analysis of the soot samples allowed the determination of the thickness of the deposited soot.

Visual inspection of the soot surface representations presented in the lower panels of **Figure 2**, and calculated as described above, reveals major differences in the distribution of CAST soot of type 1 and that of type 3 upon the substrate. While CAST-3 soot presents an even distribution of relatively constant thickness (well-defined distribution centered around 30 microns), CAST-1 soot is deposited in islands of varying height and hence exhibits a much wider distribution of soot thickness. The CAST-3-type soot also reveals smaller scale roughness (i.e. submicron; pixel width = 0.2 μm) on its surface.

The final step in the image analysis was to measure the surface area of the soot samples, determined from the soot surface representations. The surface areas of the two types of soot were calculated from the central images (X_0,Y_0) of the CAST-1 and CAST-3 soot samples by a standard triangulation method based on a summation of the triangulated areas across all pixels (X_i, Y_i, Z_i). In this method, the surface area is assumed to be represented by a net of triangles constructed assuming that a pixel's height can be attributed to its center on the X, Y plane. The derived three dimensional surface areas of CAST-1 soot and CAST-3 soot are $2.9 \pm 0.2 \times 10^4$ μm^2 and $2.3 \pm 0.2 \times 10^4$ μm^2, measured over a two-dimensional imaged area of 0.5×10^4 μm^2, i.e. 5.8 and 4.6 μm^2 per square micron, respectively. Thus, the two types of soot have a very similar surface area (factor of difference), despite the large difference in their deposition thickness distributions. Note that the fractal dimension (FD) measured by Ouf et al. (2016)[53], which represents the mass distribution within the aggregates making up soot particles (themselves composed of ultrafine carbonaceous particles), is also similar between the two samples ($FD_{CAST\text{-}1}$=1.73, $FD_{CAST\text{-}3}$=1.79). However, their density ($D_{CAST\text{-}1}$=1543 kg.m^{-3}, $D_{CAST\text{-}3}$=1321 kg.m^{-3}), crystallite lengths ($CL_{CAST\text{-}1}$=2.8 nm, $CL_{CAST\text{-}3}$=0.6 nm), and median electrical mobility diameter ($DB_{CAST\text{-}1}$=211 nm, $DB_{CAST\text{-}3}$=138 nm) are different.

It is assumed that some regions of the deposited soot will be thicker than 45 μm due to the random nature of the deposition of CAST-1 soot and the significantly longer deposition time. However, optically, the pixels become no darker and the resulting calculated surface does not vary significantly from the sample of CAST-1 soot deposited for half this length of time (**Figure 2**, upper panel). This may be due to diffuse light passing through the fluffy structure of the soot particles. This is a limitation of the measurement method which can likely not be corrected for using the current experimental setup.

RESULTS AND DISCUSSION

IDroNES: proof of concept. Deliquescence refers to the property of a salt to absorb water vapor until it dissolves completely and forms an aqueous solution. The deliquescence relative humidities (DRH) with respect to the temperature for sodium chloride salt crystals ($NaCl_{(s)}$) of a few micrometers[48-50] are well established in the literature, and show only slight variations with crystal size, in contrast to what is observed in the nanometer size-range (±10% RH)[66]. Accordingly, IDroNES is first used to monitor deliquescence processes of $NaCl_{(s)}$ (3-10 μm) and measure the DRH at 5 different temperatures. Results are plotted in **Figure 3** as the temperature at which full deliquescence is observed through the optical microscope against the corresponding RH given by the cryohygrometer. In **Figure 3**, results are also compared to those obtained by Koop et al. (2000)[49] and Wise et al. (2012)[50], and to the expected RH curve that has been extrapolated to lower temperatures by Tang and Munkelwitz (1993)[48]. **Figure 3** demonstrates that our results showing the dependency of $NaCl_{(s)}$ deliquescence relative humidity ratios with temperature are in line with those found in the literature and therefore validates IDroNES with respect to relative humidity measurements.

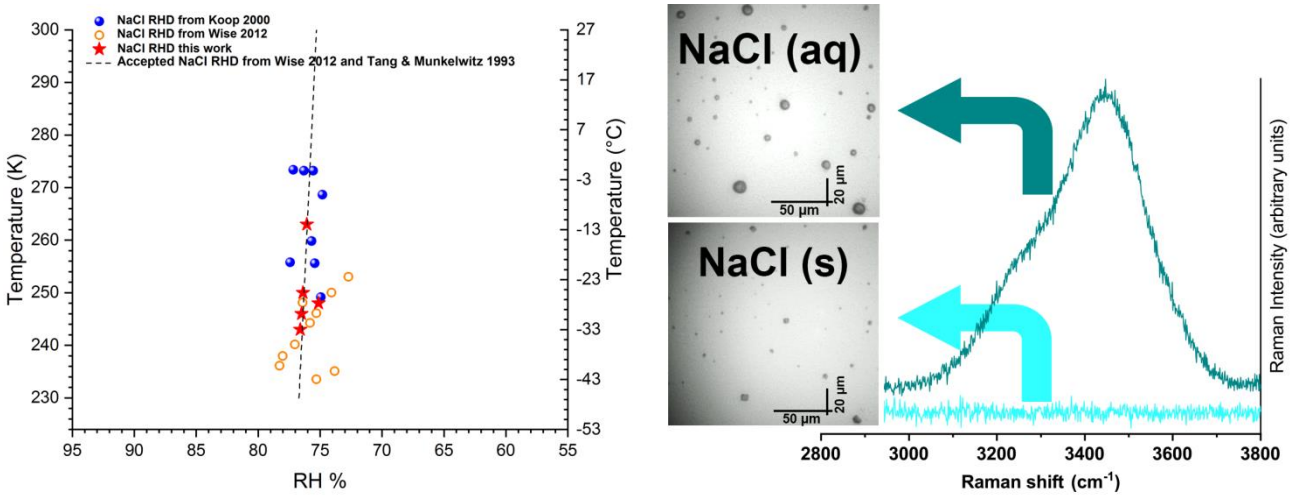

Figure 3. Deliquescence relative humidity (DRH) ratios of micrometer-sized NaCl crystals (left panel, red stars) compared to those obtained by Koop et al. (2000)[49] (blue filled circles), Wise et al. (2012)[50] (orange open circles), and the expected RH curve that has been extrapolated to lower temperatures by Tang and Munkelwitz (1993)[48] (dashed line). Optical images and Raman spectra for $NaCl_{(s)}$ and dissolved $NaCl_{(aq)}$ are shown in the right-hand side of the Figure. As expected, the Raman signature corresponding to the water O-H stretching vibration mode emerges when water is absorbed and the salt dissolves into an aqueous solution.

In addition, the optical and spectroscopic capabilities of IDroNES enable the identification of the nature of the micron-sized embryo (ice crystals or possibly supercooled water droplets) while monitoring nucleation events. It is thus possible to correlate the ice crystal habits observed on samples to the supersaturation ratio in the chamber using the well-established ice crystal habit diagram portrayed by Bailey and Hallett.[67-68] The ice crystal habit diagram plotted as a function of temperature and ice supersaturation in the work of Bailey and Hallett[68] shows that long, solid columns and polycrystals with columnar and plate-like components are expected at temperatures just below -40°C for an S_{ice} of about 1.1-1.25. An example of a solid column growing perpendicular to the microscope's focal plane in our experiment is displayed in **Figure 4**. Time lapse shots are taken over 12 min after focus adjustments in the z direction. The crystal depicted in **Figure 4** shows a solid asymmetric face from which we can measure the growth along a maximum

dimension.[67] The columnar component is rather inferred from the concomitant growth of other crystals that present a different orientation (e.g. in the microscope's focal plane) and for which the long column habit appears clearly. In addition, Raman spectra acquired across the crystal depicted in **Figure 4** were alike and confirmed the "solid" character of the column. A crystal growth rate of 0.12 $\mu m.s^{-1}$ was measured at -45°C under conditions of S_{ice} = 1.25 and P = 300 mbar. This result is in good agreement with that of Bailey and Hallett (2004)[67] who calculated a growth rate of about 0.1 $\mu m.s^{-1}$ for columns growing in a diffusion chamber at -40°C and $S_{ice} \approx 1.25$.

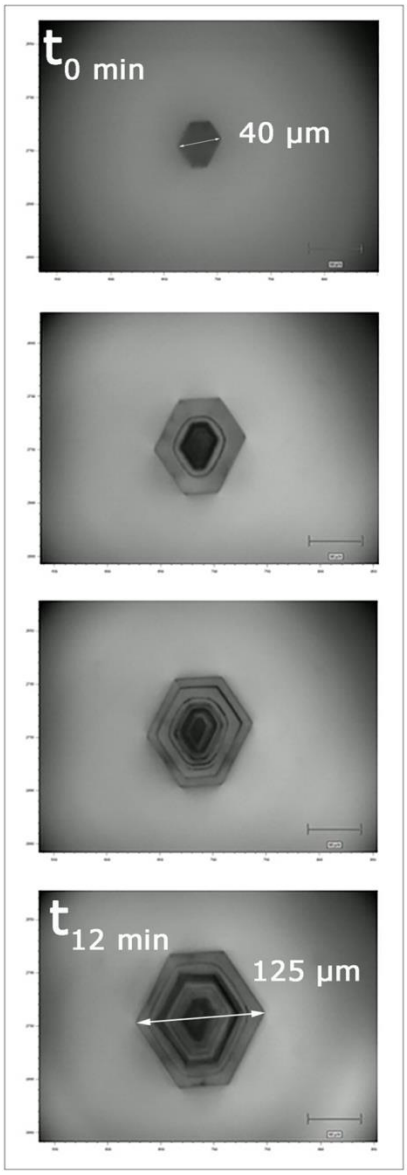

Figure 4. Optical images showing the evolution in size of the same crystal as time elapses at constant temperature and incident humid flow. Substrate is silicon, temperature -45°C, S_{ice} = 1.25, P ≈ 300 mbar.

Nucleation experiments on carbon-bearing substrates and silicon wafer. The carbonaceous samples on which ice and droplet nucleation activity have been tested are shown in **Figure 5**. Samples *a*, *c*, and *e* (CAST-3, CAST-3b, and Kero-14, respectively) exhibit a soot film showing a granular structure that cannot be resolved using the microscope. Samples *b* and *d* (CAST-1 and CAST-1b, respectively) display islands of soot particles, or clumps when the

coverage increases, with fibrous features. Note that for samples *a* to *e*, micro-Raman measurements indicate that the light grey areas surrounding the dark aggregates are also covered by a thin soot film. Conversely, the lightest grey surfaces observed on sample *f* are free of carbonaceous material. In addition, oil-like droplets arranged in ring-like patterns are visible on sample *f*. Sample *h* exhibits large light grey silicon areas devoid of soot powder since the powder has been sprinkled on the substrate. The bare silicon substrate and carbon-bearing samples *a-f* (**Figure 5**) were exposed to multiple RH scans in IDroNES between -15°C and -45°C.

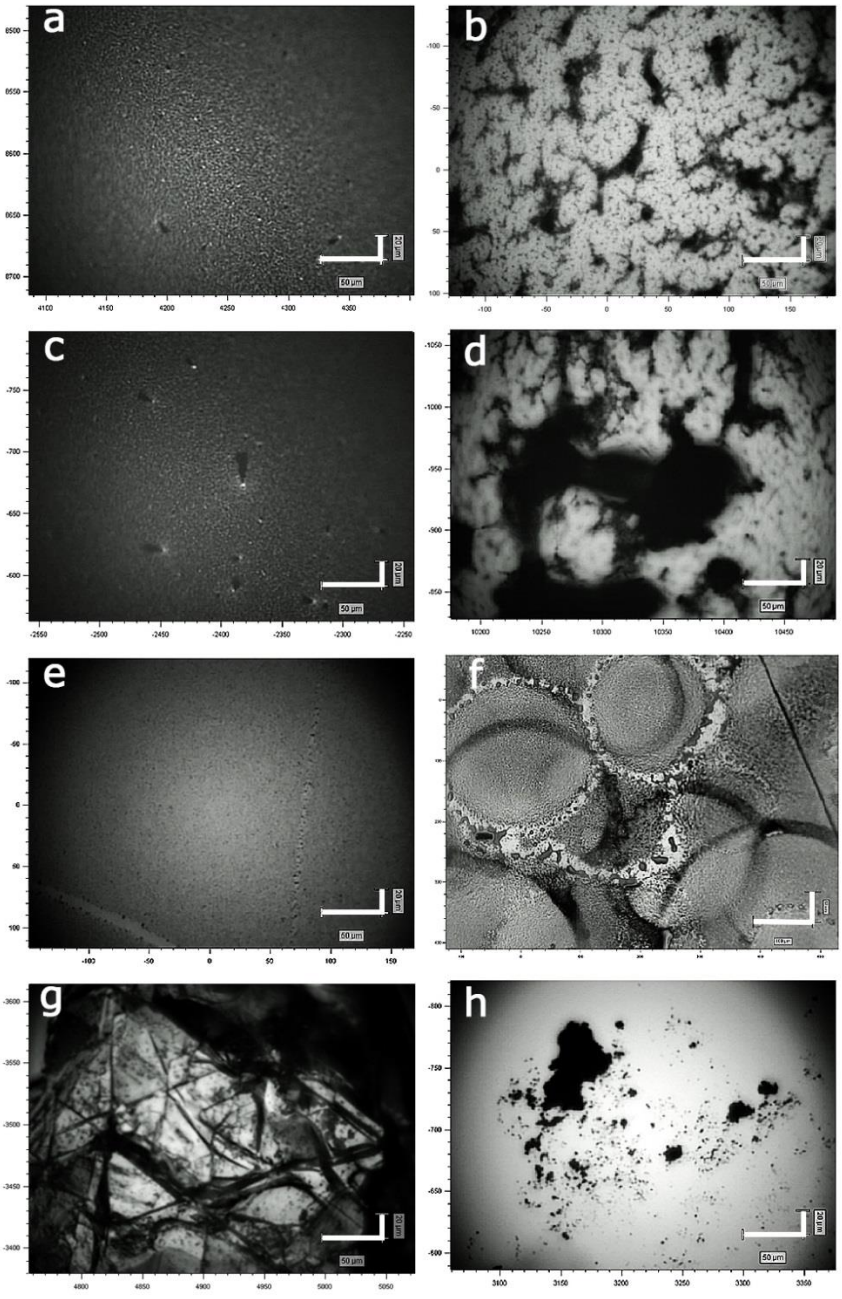

Figure 5. Optical images of carbonaceous samples whose ice nucleation activity has been measured. a) CAST-3, b) CAST-1, c) CAST-3b, d) CAST-1b, e) Kero-14, f) Kero-03, g) Graphite flake, h) CAST-3c. Images were taken with the 20x magnifier and, as such, the bottom right horizontal and vertical scale bars are 50 µm x 20 µm, respectively, except for sample f whose image was taken using the 5x magnification objective (100 µm x 50 µm).

Ice saturation ratios (S_{ice}) triggering the first observed nucleation events were subsequently derived for each studied temperature in **Figure 6**. The derived S_{ice} values presented in **Figure 6** indicate that all samples are active (S_{ice} =1.0-1.35) within the temperature range studied. In fact, the relative humidity ratios needed here to trigger ice nucleation lie below water saturation (RH_w =68-95%). Some previous experiments in deposition mode and using cloud chambers have also reported positive activities (S_{ice} ~1.1-1.3) for soot and black carbon[31, 33, 69], mostly below -38°C. While cloud chambers are used to probe ice nucleation activity on single particles or soot aggregates in the submicron range, here experiments are performed on deposited polydisperse soot particles ranging from small aggregates (Figure 4, sample *h* (1µm-70 µm)) to structured films (Figure 4, samples *a-f* are granular, fibrous, or stained with oil-like patterns). The reported S_{ice} for our most active carbon-bearing samples (S_{ice} ~1.0) are smaller than those previously reported in deposition mode for n-hexane, lamp black, furnace black, propane CAST, graphite spark generator, and acetylene soot, for which S_{ice} ~1.02-1.70 were determined using cloud chambers[25, 28, 30, 32-33, 70] or cold stages[36, 41, 70], whereby for the latter soot aggregates are deposited on a substrate akin to what is performed in our experiment. In the cirrus cloud (CC) regime (-38°C and colder), **Figure 6** shows that all carbonaceous samples tend to be more active than their silicon substrate as shown by their lower S_{ice} (note that the nucleation activity of Kero-03 was not tested at these temperatures). The S_{ice} values at which ice nucleation is observed on silicon tend to increase as the temperature gets colder (light grey area in **Figure 6**) but remain between 80-90% RH_w. In contrast, ice nucleation onsets for CAST-3, CAST-3b, CAST-1, CAST-1b, and graphite flakes are observed at RH_w below 80%, whereas that of Kero-14 lies above 85%.

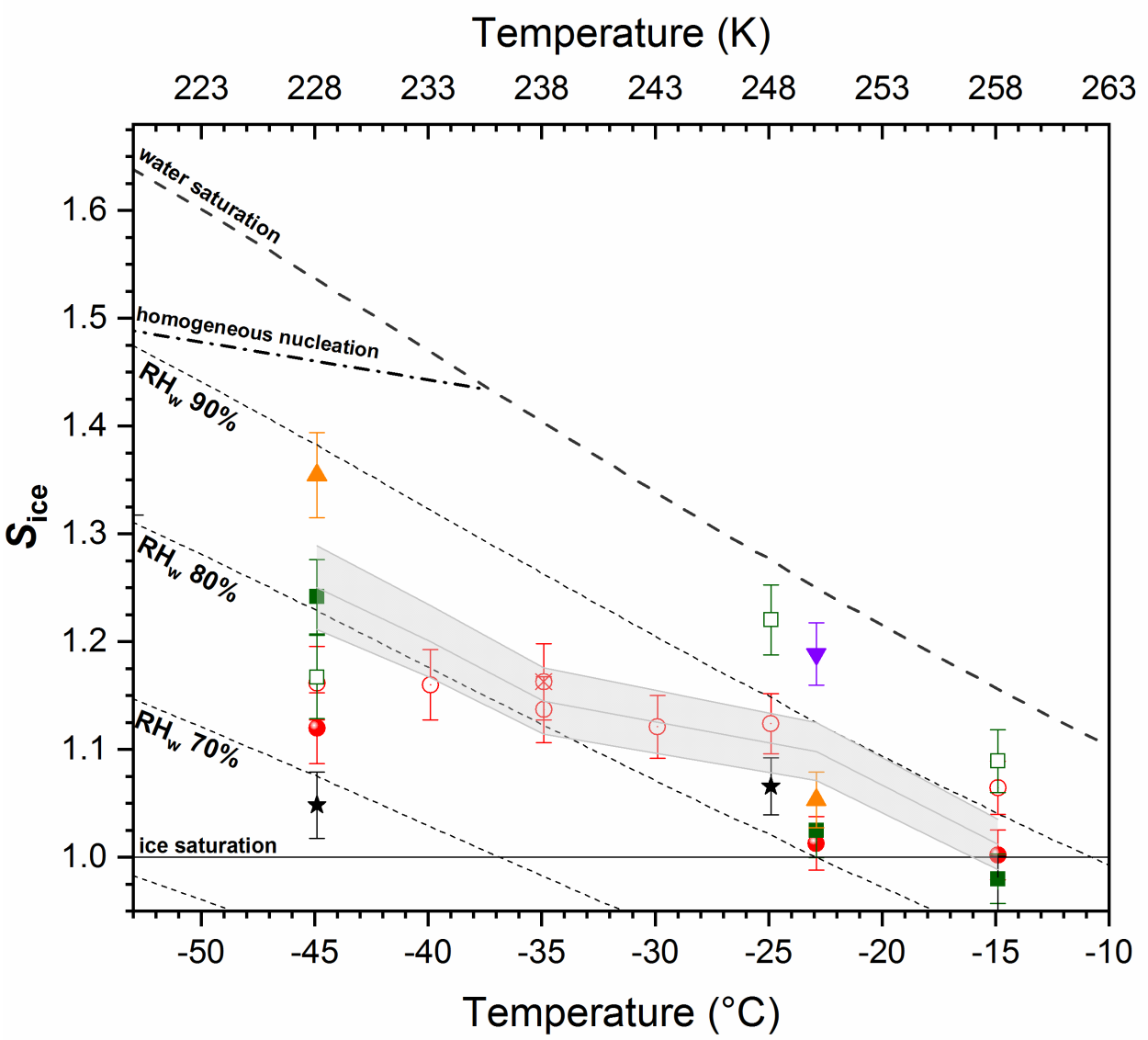

375

376 **Figure 6.** a) Ice nucleation onset temperatures (first nucleus detected) and corresponding
377 saturation ratios with respect to ice for bare silicon and carbon-bearing samples. ● CAST-3, ○
378 CAST-3b, ⊗ CAST-3c, ■CAST-1, □CAST-1b, ▼Kero-03, ▲ Kero-14,★ Graphite Flakes.
379 The light grey area shows the ice nucleation onset temperatures obtained for a bare silicon wafer.
380 The horizontal solid black line represents the ice saturation ratio at ice saturation (S_{ice} =1). The
381 bold diagonal dashed line represents the ice saturation ratio at liquid water saturation, and
382 additional relative humidity (RH) ratios with respect to water have been indicated for ease of
383 reading. The dotted-dashed isoline corresponds to the homogeneous freezing of a 200 nm solution
384 droplet.[22, 71]

385

As briefly mentioned before, representing S_{ice} as a function of temperature does not necessarily give the full picture of how active a sample can be, and may participate in large result discrepancies when cross comparing literature data. In this representation, a very low S_{ice} (reported for the first crystal detected) will define a sample as very active, as not much water vapor will be needed to trigger ice nucleation. But, by definition, this does not take into account the number of crystals which can grow over the whole surface over time. It is reasonably well established that the probability of nucleation increases with the total surface area of a particle,[72-74] because of the enhanced occurrence of active sites on larger surface areas. Yet little is still known about the specific surface properties driving the emergence of ice embryos[75] and the exact parameters giving them sufficient stability to grow to macroscopic ice.[76] Over the past few years, parametrization models have been developed to facilitate the intercomparison of results obtained with different ice nucleation detection thresholds, using a time-independent description of ice nucleation normalized to the surface area of the particle.[37, 69, 77-78] One metric often found in the literature is the ice-active surface site density (n_s), which normalize a defined activated fraction (ratio of activated particles to total number of particles) or number of ice crystals (N_{ice}) to the total surface area of polydisperse aerosols.[37, 69] In an attempt to normalize the nucleation activities solely defined in **Figure 6** by their S_{ice}, nucleation onset we also considered an approximation of n_s, whereby our derived n_s (cm^{-2}) were subsequently normalized to S_{ice} to account for the variations at different temperatures, as follows:

$$\frac{n_s}{S_{ice}} = \frac{N_{ice}}{S_{ice} A_{total}} \qquad (2)$$

With N_{ice} the number of ice crystals when S_{ice} is determined (N_{ice} =1) and A_{total} the total surface area of the sample (cm^2). The n_s/S_{ice} ratios were hence calculated uniquely for samples for which

the total surface area could be estimated. Consequently, we sought to assess surface areas of CAST-3 and CAST-1 soot samples and found them very similar for the two types of soot (a factor of ~1.3 difference), despite the large difference in their deposition thickness distributions. However, while the fractal dimension, which represents the mass distribution within the aggregates making up soot particles (themselves composed of spherical primary particles), is similar between the two samples, their density, crystallite lengths, and median electrical mobility diameter are different.[53] In addition, surfaces areas determined using BET measurements also found comparable values between that of CAST-3-like and that of CAST-1-like soot samples.[79] Samples for which specific surface areas could be estimated (silicon wafer, graphite flakes, CAST-3, and CAST-1, with 3.8, 9.5, 17, and 22 cm^2, respectively) have been tentatively normalized using equation (2). The lowest ice-active surface site density at -45°C (reflected by the lowest n_s/ S_{ice} ratio) is assigned to CAST-1 (3.7×10^{-2} cm^{-2}) as it exhibits the highest surface area among the 4 samples, closely followed by CAST-3 (5.2×10^{-2} cm^{-2}), graphite flakes (6.4×10^{-1} cm^{-2}), and eventually the silicon wafer (2.0×10^{-1} cm^{-2}). The derived n_s/ S_{ice} ratios for such CAST soot films are significantly lower compared to what has been previously reported in the literature for individual soot particles or small soot aggregates (10^4-10^9 cm^{-2})[37, 69] within a similar temperature range (between -50°C and -40°C). This is the result of the large surface area probed in this experiment i.e. that of the entire particle population collected on the substrate. In addition, the threshold of detection (first crystal detected with our optical resolution) is only a snapshot taken at the early stage of nucleation and growth processes (since N_{ice} =1) and the exact surface area available to water molecules is not accessible as our optical surface reconstruction does not reflect nanoscale roughness/porosity variations that could, if taken into account, further segregate CAST-1 and CAST-3 soot samples. In addition, the first crystal detected can act as sink for water molecules and hence will strongly

compete with any other active sites present on the surface to attract water molecules. As the ice nucleation activity occurs here on large samples (high particles number or high specific surface area), low n_s values are not irreconcilable with low S_{ice} values (recorded when the first crystal is detected) as more (and possibly better)[77] active sites are likely to be available on large surfaces compared to smaller surface (e.g. individual soot particle). The ice nucleation onset hence only reflects the highest activity among all active sites over the whole sample surface.

In the mixed-phase cloud (MPC) regime (warmer than -38°C), the derived S_{ice} values may not always appear statistically different from that of the blank. However, a combination of the optical images with the derived S_{ice} can further help in inferring the original location of the first crystal. **Figure 7** shows a set of optical images illustrating some of the nucleation events for which S_{ice} values were reported in **Figure 6**. For instance, it is clear from the sequence *f-f''* in **Figure 7** that the ice crystal has grown on CAST-3c even though a large area of bare silicon surrounds the clump of powder, area that would be very competitive in hosting this event if the ice nucleation event had not been heterogeneously triggered by the soot. Additional in-situ observations through the microscope show that ice crystals grow evenly on CAST-3, CAST-3b, and Kero-14 (where a soot film showing a granular structure covers the surface), but preferentially grow on particle aggregates for CAST-1 (i.e. on the fibrous soot islands), CAST-1b (fibrous clumps) and graphite flakes (**Figure 7**). This supports the fact that soot samples CAST-3, 3b, 1, and 1b, as well as graphite, do nucleate ice before the substrate onto which they are deposited. Among all tested soot samples, Kero-03 and CAST-1b exhibit ice nucleation events around -25°C at RH_w>90%, i.e. closer to that of water saturation (which make them the least active samples at this temperature in terms of S_{ice} at the ice nucleation onset). As CAST-1 and CAST-3 roughly exhibit the same surface area for water molecules to interact with, but need different S_{ice} to trigger ice nucleation, it is likely

454 the distinct chemical composition of the two CAST samples and/or their distinct surface
455 topography that yield this difference. Consequently, these two parameters have been investigated
456 and are discussed below.

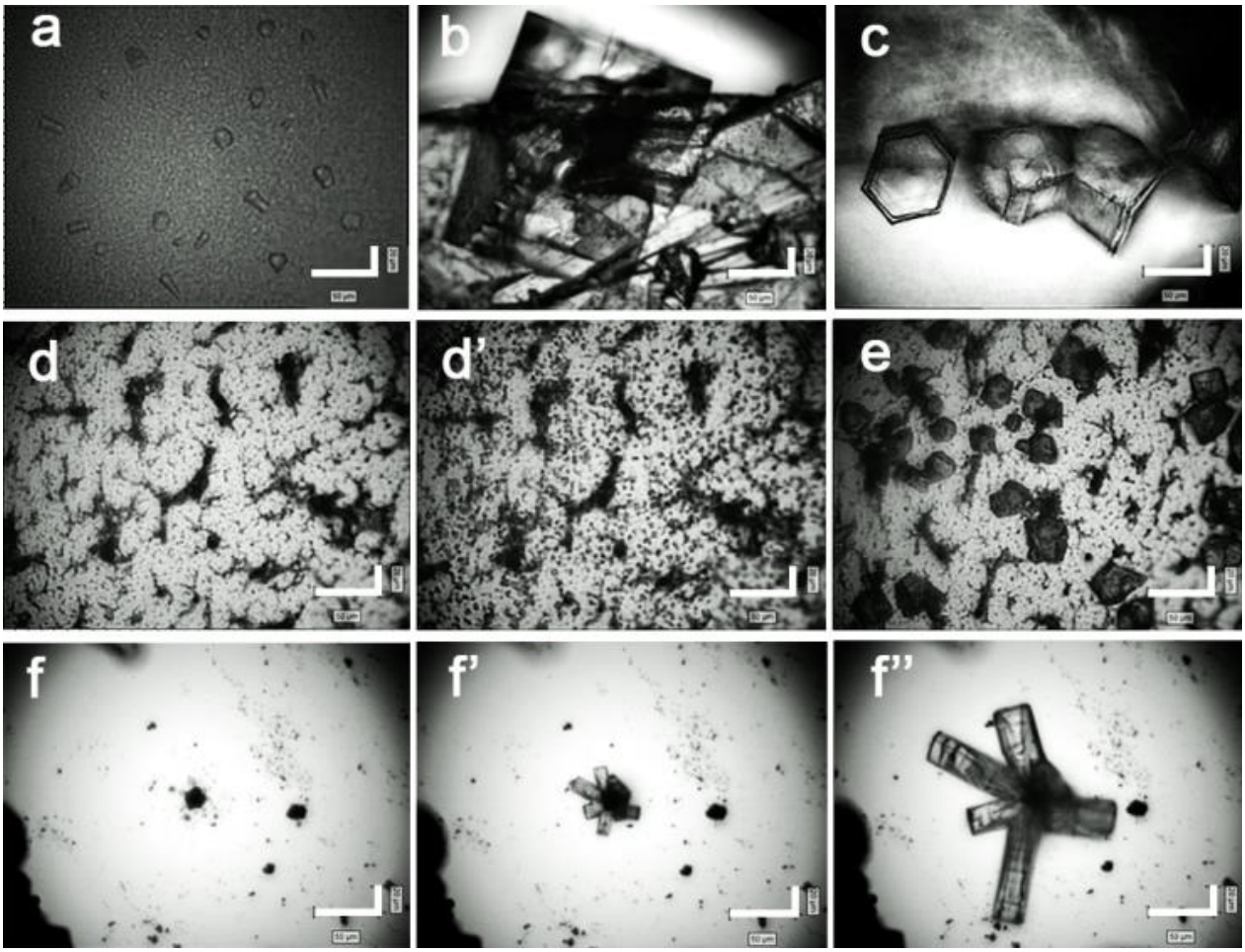

457

458 **Figure 7.** Optical images taken during nucleation events showing ice crystals growing on a)
459 CAST-3 at -45°C, b) graphite flake at –35°C and c) at –45°C. Images d) and e) show CAST-1 and
460 preferential crystal growth on soot islands at -55 and -45°C, respectively, and image f) on CAST-
461 3c. The prime and double prime symbols show time lapse pictures of the same areas: time elapses
462 from left to right.

463

464 **Influence of sample surface composition**. The chemical composition of propane soot
465 samples produced with the same miniCAST set points have been investigated in the past.[54 53, 80-83]

The two soot samples CAST-3 and CAST-1 differ in their bulk organic to total carbon (OC/TC) ratios, being high and low, respectively. The OC/TC ratios for samples CAST-3 and CAST-1 were determined using a conventional thermo-optical method to be about 87% and 4%, respectively.[53, 84] The first striking result is that soot samples CAST-3b and Kero-14, which contain the most polycyclic aromatic hydrocarbons (PAHs), trigger ice nucleation in average at lower S_{ice} than their counterparts do (S_{ice} (CAST-3, CAST-3b, Kero-14) ≤ S_{ice} (CAST-1, CAST-1b, Kero-03) over the whole temperature range studied. While the surface area of Kero-14 and Kero-3 soot samples could not be evaluated and therefore no n_s/S_{ice} ratio could be subsequently derived and compared to those of CAST-3 and CAST-1, both CAST soot samples exhibit ice-active surface site density of the same order of magnitude, but their S_{ice} are different, with S_{ice} (CAST-3) < S_{ice} (CAST-1). This observation appears at first to be in disagreement with the work of Ullrich et al. (2017)[69] and Crawford et al. (2011)[30] (**Table 1**), where uncoated CAST propane soot particles of low organic carbon contents (~5%) were found to be more active at nucleating ice than soot with higher organic contents (30-90%). In fact, the authors[69] reported the S_{ice} obtained at the start of ice nucleation and showed an increase of S_{ice} with the samples' bulk organic content (**Table 1** and **SI**). However, this bulk parameter does not necessarily reflect the surface chemical composition of the particles, i.e. the part directly interacting with water vapor.

Table 1. Ice saturation ratios (S_{ice}) at the nucleation onset (deposition mode) for different CAST propane soot samples in the cold temperature regime.

Burner Type/Name	**OC/TC (%)**	**Round nearest nucleation temperature (°C)**	S_{ice}	**Ref**
CAST	5	-41	1.19	[69]
CAST	5	-46	1.25[a]	[30]
CAST-1	4	-45	1.14	This work
miniCAST	30	-48	1.33[a]	[30]
CAST	60	-49	1.50[a]	[30]
CAST-3	87	-45	1.16	This work
miniCAST	90	-	-[b]	[30]

485 [a]S_{ice} determined at 1% activation which represents the fraction of aerosols that becomes ice active, [b]No
486 heterogeneous ice nucleation observed.

487 Consequently, we characterized the nature of the organics making up the samples' surfaces using
488 mass spectrometry techniques. Our surface analyses clearly highlighted that the 'organic content'
489 referred to in bulk analyses[53, 56, 84] can be identified as being a mixture of PAHs. However, it is
490 also clear that different features appear for the two CAST soot type of samples (**Figure 8**), where
491 PAHs are distinct in their nature and quantity. CAST-3 soot has a total surface PAH content
492 significantly higher than that of CAST-1 soot (for the same surface area analyzed), and further
493 exhibits a surface PAH mass distribution (SIMS) shifted to higher masses compared to that of
494 CAST-1 soot. In addition, although bulk Fourier transform infrared spectrometry (FTIR)
495 analyses[54] detected the presence of alkanes and alkenes in both CAST-1 and CAST-3, here only
496 CAST-1 soot surface exhibits L2MS signatures corresponding to saturated hydrocarbons (alkanes)
497 and alkyl-PAH. Our L2MS results are in line with the work of Moore et al. (2014)[82] where the
498 PAH to soot ratio is shown to decrease with the oxidation airflow rate generating the soot particles:
499 CAST-3-like soot contains more PAHs than CAST-1-like soot and we additionally show that they
500 are of different nature.

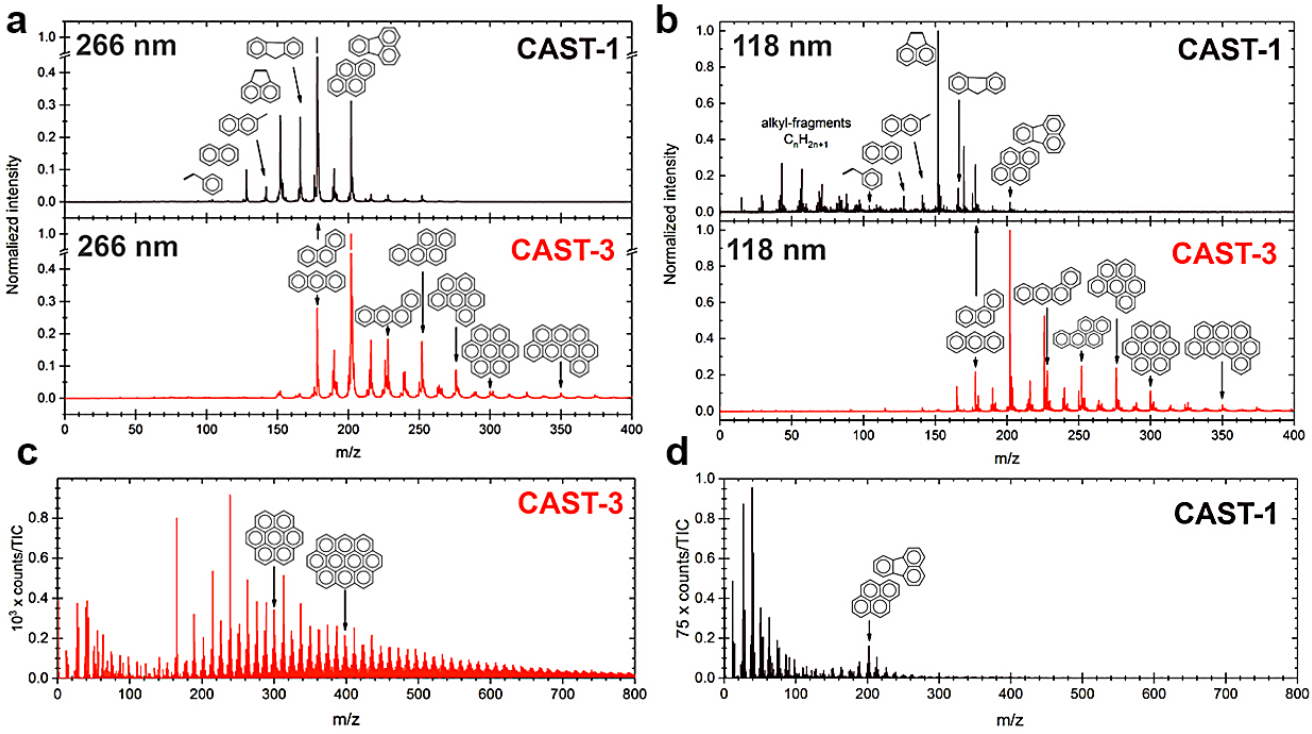

Figure 8. Mass spectra of CAST soot samples 3 and 1. L2MS desorption wavelength is 532 nm and ionization wavelength is a) 266 nm, and b) 118 nm. Selected L2MS peak assignments (selected isomers, contributions from other isomers are possible) for CAST-1: 104 *m/z*: styrene, 128 *m/z*: naphthalene, 142 *m/z*: methylnaphthalene (or isomers), 152 *m/z*: acenaphthylene, 166 *m/z*: fluorene, 202 *m/z*: pyrene or fluoranthene, for CAST-3: 178 *m/z*: phenanthrene or anthracene, 228 *m/z*: benzo[a]anthracene, 252 *m/z*: benzo[a]pyrene, 300 *m/z*: coronene, 350 *m/z*: benzo[lmn]naphtho[2,1,8-qra]perylene. c) and d) SIMS spectra. Selected SIMS peak assignments for CAST-1:202 *m/z*: pyrene or fluoranthene, for CAST-3: 300 *m/z*: coronene, 398 *m/z*: ovalene.

In addition, Ouf et al.(2016)[53] showed that the oxygen content (in atomic percent) reaches about 10 at% and 4 at% for CAST-3 and CAST-1, respectively, and they attributed this observation to the better accessibility of oxidizing molecules to the edge sites of poorly ordered crystallites such as those found in CAST-3, as opposed to the more ordered structure of CAST-1. Although CAST-3 shows a higher OC/TC content than CAST-1, it also bears larger PAHs and more oxygenated moieties than CAST-1. An increased oxidation or functionalization of surface-bound species is known to support water uptake and facilitate nucleation,[27, 46, 82, 85-86] and may play a role

here in lowering S_{ice} for the highest OC/TC ratio (CAST-3, **Figure 6**). On the other hand, while PAH are known to exhibit an overall negligible solubility in water, variations with the PAHs' molar volumes[87] are observed. For instance, small PAHs and alkyl-PAHs such as those found on CAST-1 are shown to exhibit higher solubility[88] than larger and unbranched PAHs, and thus surface species on CAST-1 may be more hygroscopic than those of CAST-3 at moderate temperatures (MPC regime), even though such property may not be as relevant for nucleation mechanisms involving vapor deposition. Finally, specific carbonaceous species or organic layers making up the distinct surfaces of CAST soot samples might, in such cases, interact with water molecules such that the interactions are neither too weak nor too strong, and hence locally provide an optimum template that can promote ice nucleation.[89] The nucleation site observed on the clump of CAST-3c powder in **Figure 7** in the *f-f''* sequence may be further indicative of the presence of surface chemical groups aiding nucleation. However, micro-Raman spectroscopy revealed no significant difference with other CAST-3c powder islands on which ice crystals were not observed, although this technique is not really sensitive to chemical functional groups for such complicated materials but rather to the nanostructure, which appears homogeneous across the sample. It is therefore still possible that a compositional heterogeneity may account for preferential water adsorption onto specific particles since the powder was mechanically removed from its filter and subsequently sown on silicon.

Similarly, mass spectra (SIMS) for Kero-03 and -14 are rich in heavy PAHs and are characterized by two mass distributions with fragments centered below *m/z* 120 and around $C_{19}H_{11}^{+}$(*m/z* 239) for the low and high mass component, respectively. Kero-14 exhibits a higher PAH content than Kero-03 in the high mass region and is made up of the heaviest PAHs (up to $C_{38}H_{16}^{+}$ (*m/z* 472), L2MS, **SI**). In addition, while signatures of oxygenated aromatics arose in both

spectra, no aliphatic compounds were detected in either. As Kero-03 was collected below the soot inception region, it exhibits several ring-like patterns at its surface that are indicative of fuel droplets exposure during collection. In contrast, Kero-14 was collected close to the mature soot zone where gas-phase PAHs have aggregated and formed soot particles, and is therefore chemically (in terms of PAHs size) closer to the CAST-3 soot sample than Kero-03 is, which may explain why Kero-14 triggers ice nucleation at a S_{ice} lower than that of Kero-03 at -23°C. Note that even though Kero-03 exhibits small PAHs like CAST-1, these are not branched. This may also account for their slight difference in activity, with Kero-03 being the less active of the two in terms of S_{ice} at the ice nucleation onset. A previous study[90] showed the high hydrophobic character of kerosene flame soot stemming from the combustion of TC1 kerosene fuel in a wick oil lamp, whereby only few water monolayers were measured to absorb onto the soot surface when exposed to RH_w <93%, which reflects a low n_s and a low ice activated fraction (30% at 240 K). Our apparent higher activity, due to a low S_{ice} obtained at the ice nucleation onset – i.e. for a very low activated fraction corresponding to first crystal detected across the whole soot sample– does not necessarily contradict the previous study, especially if water molecules preferentially form clusters[90] once they have found an active site. Nevertheless, we stress the differences in both the fuel and the burner used within this study, which result in different combustion conditions that may affect[91] both the amount of oxygenated particles and the saturation of the aliphatic species, and thus may account for possible differences in activities. Such compositional variance probably also drives the difference in S_{ice} at the ice nucleation onset between Kero-03 and Kero-14. However, as their respective surface areas could not be derived, their activity in terms of n_s could not be evaluated.

Influence of topography. Besides a possible difference in surface areas, an uneven particle collection at the surface or the particles themselves can display nano to microscale pores, cracks,

564 and pits. Such surface asperities might also play a role in reducing the S_{ice} needed to trigger ice
565 nucleation upon water vapor exposure. Accordingly, we appraised the influence of the pore
566 condensation and freezing (PCF) mechanism,[92-100] whereby water vapor can condense in voids and
567 cavities (capillary condensation due to the concavity of the water surface in a pore) and
568 subsequently freeze (homogeneously, when the confined droplets have grown large enough for the
569 solid phase to be stable from a thermodynamic standpoint), provided the temperature is sufficiently
570 low (below -38°C). Aerosols exhibiting pores within the 3-8 nm range may contain ice due to the
571 PCF mechanism even in cold subsaturated environments with respect to water (e.g. for S_{ice} ~0.84
572 at - 47°C considering a pore diameter of about 8 nm).[99] For soot particles, capillary condensation
573 presumably occurs in the voids or cavities between aggregated primary particles.[96] Since both
574 CAST-1 and CAST-3 show a wide height distribution, we conjecture that they also encompass a
575 large number of cavities in which PCF might take place. Mahrt and coworkers[40] demonstrated that
576 soot aggregates containing mesopores (2-50 nm) with sufficiently low water-soot contact angles
577 could exhibit ice nucleation activities well below the RH needed for the homogeneous freezing of
578 a solution droplet in the CC regime. However, a rough approximation of the CAST soot samples'
579 pore sizes using their hydraulic diameter as a proxy[101-103] (see SI for details) indicates they might
580 be larger than the size regime for where PCF is observed to occur (i.e. >11 nm,[99] with a diameter
581 of primary particles[53] similar for CAST-1 and CAST-3 soot of about 30 nm, both forming
582 aggregates with micron-sized pores). This suggests that PCF does not prevail here and that the
583 observed ice nucleation stems straight from vapor deposition.

584 Bare highly oriented pyrolytic graphite (HOPG) is usually described as an inefficient substrate
585 for ice nucleation due to its low wettability, i.e. graphite-water interactions are weaker than water-
586 water interactions, which results in the growth of rough ice surfaces rather than smooth crystalline

ice surfaces at water supersaturations.[104-105] In contrast, in graphite samples exhibiting structural defects such as graphites flakes (see **Figure 5-g**), small-scale landscape geometry considerations such as the presence of wedges, pits, cracks, or loose small aggregates would reduce the thermodynamic free energy barrier to nucleation directly from vapor and may participate in reducing the S_{ice}.[106] Graphite flakes such as those studied here optically clearly show the presence of micron-sized surface defects (**Figure 5-g**). Further Raman analyses highlighted the existence of disorder bands (D and D') in our sample (see SI for details), indicative of the presence of small graphene sheets or/and holes vacancies[51, 107] that create reactive edges, which can facilitate nucleation and explain the low S_{ice} found for graphite flakes in our experiments. Similarly, Kanji et al. (2011)[29] found graphite spark generator soot particles (mostly elemental carbon) efficient IN at temperatures colder than -39°C (S_{ice} ~1.27-1.36), whereas the same soot particles needed water saturation to nucleate above -37°C. Here, no such distinct behavior has been observed for graphite flakes; they are active (in terms of S_{ice}) but exhibit a very low n_s when normalized to the surface available for ice nucleation to occur throughout the whole temperature range.

CONCLUSION

We built an experimental setup (IDroNES) to monitor in-situ deposition nucleation processes subsequently followed by ice growth on particles using optical and spectroscopic detections. We tested IDroNES by first, monitoring the deliquescence relative humidities of $NaCl_{(s)}$ micron-sized crystals and second, by performing optical measurement of crystal habits and crystal growth at a given S_{ice}. Once IDroNES was validated, we probed the nucleation activity of carbon-bearing samples of various surface chemical compositions, morphologies and surface areas, from soot powder to soot films, including graphite flakes, in the -15°C to -45°C temperature range.

We found all tested samples active at nucleating ice crystals when exposed to humid nitrogen (in terms of ice saturation ratio S_{ice} reported at the ice nucleation onset such as detected with our optical resolution). CAST-3 soot yielded the lowest S_{ice} throughout the whole studied temperature range. In an attempt to derive ice-active surface site densities (n_s) which require the knowledge of the sample surface area available to water molecules, we developed an optical method to reconstruct CAST soot films surface features and assess surface areas. For selected data we were then able to derive n_s for very large surface areas. All selected samples (CAST-1, CAST-3, graphite, and silicon substrate) yield very low n_s, i.e. for a range of surface areas that remained largely unexplored to date. Despite the large surface areas of most tested samples, distinct S_{ice} and n_s suggest that the surface chemical composition and morphology likely play a role in discriminating samples as to their ice nucleation activity.

In order to investigate to role of surface chemistry in ice nucleation, we performed two-step laser mass spectrometry (L2MS) and secondary ion mass spectrometry (SIMS) measurements. L2MS measurements were performed using two ionization wavelengths (266 nm and 118 nm) to target various classes of compounds (i.e. polycyclic aromatic hydrocarbons (PAHs) or saturated hydrocarbons (alkanes)). These analyses indicated that the surfaces of the two CAST set points investigated in this work (CAST-1 and CAST-3) consist mainly of PAHs that are distinct in nature for the two samples, i.e. the PAH mass distribution is shifted to higher masses for CAST-3 soot compared to CAST-1 soot. In addition, the total surface PAH content is significantly higher for CAST-3 soot, while previous measurements additionally showed that CAST-3 soot contained also the most oxygen in atomic percent.[53]

In conjunction with different surface chemistries, the carbon-bearing samples also exhibit morphological variabilities. Optical images acquired for CAST and graphite soot samples showed

distinct micron-sized features, some exhibiting soot clumps (CAST-1) or a relatively smooth granular surface (CAST-3), or even cracks and pits (graphite flakes). Although organic coatings on soot particles usually lower the ice nucleation activity, the combined effects of surface chemical composition with different surface areas and morphologies (roughness, cracks, pores, particle size, or other structural defects of any kind at possibly different size scales) may result in the overall higher activity than that expected when considering the surface composition alone. As the various surface chemistries are intertwined with the morphological character of the particles, the individual effect of each parameter cannot be deciphered in this work.

ASSOCIATED CONTENT

Supporting Information. Supporting information (SI) in the form of a PDF is available free of charge. The SI provides details (2 Texts, 7 Figures, and 2 Tables) on how our samples were produced (Table S1), provides the reader details on the optical technique we developed to represent our sample surface areas (Figures S1-S8), shows the Raman signatures of micron-sized ice crystals that have grown on various substrates and that of a supercooled droplet at -15°C (Figure S5), and on how the porosity of our samples has been assessed using their hydraulic diameter as a proxy (Table S2).

AUTHOR INFORMATION

Corresponding Author

*Claire Pirim: claire.pirim@univ-lille.fr

Present Addresses

† CNRS, Aix Marseille Université, PIIM, UMR 7345, 13397 Marseille cedex, France

‡ Department of Multi-physics for Energetics, ONERA Université Paris Saclay, F-91123, Palaiseau, France

Author Contributions

RI, CP, and BC conceptualized and built IDroNES; RI and CP processed the samples in IDroNES; CP and JAN conceptualized and developed the optical surface measurement method, CI, YC, and IKO performed mass spectrometry analyses, RI and CP performed Raman spectroscopy analyses,

FXO provided the miniCAST samples and performed soot porosity calculations, RI, CP, JAN, BC, YC, CI, and CF interpreted the results; RI and CP wrote the original draft with additional contributions from other co-authors: JAN, YC, CI, IKO, FXO, CF, and BC. BC and CF provided funding and CF access to the experimental SIMS infrastructure. All co-authors reviewed and approved the manuscript. All authors have given approval to the final version of the manuscript.

ACKNOWLEDGMENT

This work was supported by the MERMOSE project for the characterization of emissions by aircraft engines and sponsored by DGAC (French national funds; http://sites.onera.fr/MERMOSE/en), by the CaPPA project (Chemical and Physical Properties of the Atmosphere) funded by the French National Research Agency (ANR) through the PIA (Programme d'Investissement d'Avenir) under contract ANR-11-LABX-0005-01, and by the Région Hauts-de-France, and the Ministère de l'Enseignement Supérieur et de la Recherche (CPER Climibio) and the European Fund for Regional Economic Development (FEDER). The authors acknowledge N. Nuns for his support in acquiring the SIMS data and E. Therssen for supplying the McKenna burner used for the collection of kerosene soot samples.

ABBREVIATIONS

IDroNES Ice and Droplet Nucleation Experimental Setup, CC Cirrus Cloud, MPC Mixed-phase Cloud, CCN cloud condensation nuclei, INPs ice nucleating particles, S_{ice} Ice saturation ratio, RH Relative Humidity ratio, DRH Deliquescence Relative Humidities, n_s ice-active surface site density, miniCAST Miniature Condensation Aerosol Standard, L2MS two-step laser mass spectrometry, SIMS secondary ion mass spectrometry, PAH polycyclic aromatic hydrocarbons, PCF condensation and freezing.

REFERENCES

1. Paoli, R.; Shariff, K., Contrail Modeling and Simulation. *Annu. Rev. Fluid Mech*. **2016**, 48, 393-427.

2. Masiol, M.; Harrison, R. M., Aircraft Engine Exhaust Emissions and Other Airport-Related Contributions to Ambient Air Pollution: A Review. *Atmos. Environ*. 2014, 95, 409-455.

3. World Airport Traffic Forecasts 2017–2040; Aeroports Council International (ACI) World: Montreal, Quebec, **2017**.

4. Kinsey, J. S.; Dong, Y.; Williams, D. C.; Logan, R., Physical Characterization of the Fine Particle Emissions from Commercial Aircraft Engines During the Aircraft Particle Emissions Experiment (Apex) 1–3. *Atmos. Environ*. **2010**, 44, 2147-2156.

5. Delhaye, D., et al., The Mermose Project: Characterization of Particulate Matter Emissions of a Commercial Aircraft Engine. *J. Aerosol. Sci*. **2017**, 105, 48-63.

6. Brasseur, G. P., et al., Impact of Aviation on Climate FAA's Aviation Climate Change Research Initiative (ACCRI) Phase II. *Bull. Amer. Meteorol. Soc*. **2016**, 97, 561-583.

7. Petzold, A.; Ström, J.; Ohlsson, S.; Schröder, F. P., Elemental Composition and Morphology of Ice-Crystal Residual Particles in Cirrus Clouds and Contrails. *Atmos. Res.* **1998**, 49, 21-34.

8. Popovitcheva, O. B.; Persiantseva, N. M.; Trukhin, M. E.; Rulev, G. B.; Shonija, N. K.; Buriko, Y. Y.; Starik, A. M.; Demirdjian, B.; Ferry, D.; Suzanne, J., Experimental Characterization of Aircraft Combustor Soot: Microstructure, Surface Area, Porosity and Water Adsorption. *Phys. Chem. Chem. Phys*. **2000**, 2, 4421-4426.

9. Demirdjian, B.; Ferry, D.; Suzanne, J.; Popovicheva, O. B.; Persiantseva, N. M.; Shonija, N. K., Heterogeneities in the Microstructure and Composition of Aircraft Engine Combustor Soot: Impact on the Water Uptake. *J. Atmos. Chem*. **2007**, 56, 83-103.

10. Vander Wal, R. L.; Bryg, V. M.; Huang, C.-H., Aircraft Engine Particulate Matter: Macro-Micro- and Nanostructure by HRTEM and Chemistry by XPS. *Combust. Flame* **2014**, 161, 602-611.

11. Kleine, J.; Voigt, C.; Sauer, D.; Schlager, H.; Scheibe, M.; Jurkat-Witschas, T.; Kaufmann, S.; Kärcher, B.; Anderson, B. E., In Situ Observations of Ice Particle Losses in a Young Persistent Contrail. *Geophys. Res. Lett.* **2018**, 45, 13,553-13,561.

12. Kärcher, B., Formation and Radiative Forcing of Contrail Cirrus. *Nat. Commun*. **2018**, 9, 1824.

13. Schröder, F.; Kärcher, B.; Duroure, C.; Ström, J.; Petzold, A.; Gayet, J.-F.; Strauss, B.; Wendling, P.; Borrmann, S., On the Transition of Contrails into Cirrus Clouds. *J. Atmos. Sci.* **2000**, 57, 464-480.

14. Zhou, C.; Penner, J. E., Aircraft Soot Indirect Effect on Large-Scale Cirrus Clouds: Is the Indirect Forcing by Aircraft Soot Positive or Negative? *J. Geophys. Res.: Atmos.* **2014**, 119, 11,303-11,320.

15. Hendricks, J.; Karcher, B.; Lohmann, U.; Ponater, M., Do Aircraft Black Carbon Emissions Affect Cirrus Clouds on the Global Scale? *Geophys. Res. Lett.* **2005**, 32, L12814.

16. Rap, A.; Forster, P. M.; Jones, A.; Boucher, O.; Haywood, J. M.; Bellouin, N.; De Leon, R. R., Parameterization of Contrails in the UK Met Office Climate Model. *J.Geophys. Res.* **2010**, 115, D10205.

17. Frömming, C.; Ponater, M.; Burkhardt, U.; Stenke, A.; Pechtl, S.; Sausen, R., Sensitivity of Contrail Coverage and Contrail Radiative Forcing to Selected Key Parameters. *Atmos. Environ*. **2011**, 45, 1483-1490.

18. Duda, D. P.; Minnis, P.; Khlopenkov, K.; Chee, T. L.; Boeke, R., Estimation of 2006 Northern Hemisphere Contrail Coverage Using Modis Data. *Geophys. Res. Lett*. **2013**, 40, 612-617.

19. Ponater, M.; Marquart, S.; Sausen, R., Contrails in a Comprehensive Global Climate Model: Parameterization and Radiative Forcing Results? *J. Geophys. Res.: Atmos.* **2002**, 107, D134164.

20. Sausen, R.; Isaksen, I.; Grewe, V.; Hauglustaine, D.; Lee, D. S.; Myhre, G.; Köhler, M. O.; Pirati, G.; Schumann, U.; Stordal, F.; Zeferos, C., Aviation Radiative Forcing in 2000: An Update on IPCC (1999). *Meteorol. Z.* **2005**, 14, 555-561.

21. Kärcher, B.; Burkhardt, U.; Bier, A.; Bock, L.; Ford, I. J., The Microphysical Pathway to Contrail Formation. ? *J. Geophys. Res.: Atmos.* **2015**, 120, 7893-7927.

22. Hoose, C.; Mohler, O., Heterogeneous Ice Nucleation on Atmospheric Aerosols: A Review of Results from Laboratory Experiments. *Atmos. Chem. Phys.* **2012**, 12, 9817-9854.

23. Diehl, K.; Mitra, S. K., A Laboratory Study of the Effects of a Kerosene-Burner Exhaust on Ice Nucleation and the Evaporation Rate of Ice Crystals. *Atmos. Environ*. **1998**, 32, 3145-3151.

24. Fornea, A. P.; Brooks, S. D.; Dooley, J. B.; Saha, A., Heterogeneous Freezing of Ice on Atmospheric Aerosols Containing Ash, Soot, and Soil. *J.Geophys. Res.* **2009**, 114, D13201.

25. DeMott, P. J., An Exploratory Study of Ice Nucleation by Soot Aerosols. *J. Appl. Meteorol.* **1990**, 29, 1072-1079.

26. Kireeva, E. D.; Popovicheva, O. B.; Persiantseva, N. M.; Khokhlova, T. D.; Shonija, N. K. J. C. J., Effect of Black Carbon Particles on the Efficiency of Water Droplet Freezing. *Colloid J.* **2009**, 71, 353-359.

27. Popovicheva, O.; Kireeva, E.; Persiantseva, N.; Khokhlova, T.; Shonija, N.; Tishkova, V.; Demirdjian, B., Effect of Soot on Immersion Freezing of Water and Possible Atmospheric Implications. *Atmos. Res.* **2008**, 90, 326-337.

28. Gorbunov, B.; Baklanov, A.; Kakutkina, N.; Windsor, H. L.; Toumi, R., Ice Nucleation on Soot Particles. *J. Aerosol. Sci.* **2001**, 32, 199-215.

29. Kanji, Z. A.; DeMott, P. J.; Mohler, O.; Abbatt, J. P. D., Results from the University of Toronto Continuous Flow Diffusion Chamber at Icis 2007: Instrument Intercomparison and Ice Onsets for Different Aerosol Types. *Atmos. Chem. Phys.* **2011**, 11, 31-41.

30. Crawford, I.; Möhler, O.; Schnaiter, M.; Saathoff, H.; Lui, D.; McMeeking, G.; Linke, C.; Flynn, M.; Bower, K.N., Connolly, P.J.; Gallagher, M.W.; Coe, H., Studies of Propane Flame Soot

Acting as Heterogeneous Ice Nuclei in Conjunction with Single Particle Soot Photometer Measurements. *Atmos. Chem. Phys.* **2011**, 11, 9549-9561.

31. DeMott, P. J.; Chen, Y.; Kreidenweis, S. M.; Rogers, D. C.; Sherman, D. E., Ice Formation by Black Carbon Particles. *Geophys. Res. Lett.* **1999**, 26, 2429-2432.

32. Koehler, K. A.; DeMott, P. J.; Kreidenweis, S. M.; Popovicheva, O. B.; Petters, M. D.; Carrico, C. M.; Kireeva, E. D.; Khokhlova, T. D.; Shonija, N. K., Cloud Condensation Nuclei and Ice Nucleation Activity of Hydrophobic and Hydrophilic Soot Particles. *Phys. Chem. Chem. Phys.* **2009**, 11, 7906-7920.

33. Möhler, O.; Linke, C.; Saathoff, H.; Schnaiter, M.; Wagner, R.; Mangold, A.; Krämer, M.; Schurath, U., Ice Nucleation on Flame Soot Aerosol of Different Organic Carbon Content. *Meteorol. Z.* **2005**, 14, 477-484.

34. Möhler, O., et al., Effect of Sulfuric Acid Coating on Heterogeneous Ice Nucleation by Soot Aerosol Particles. *J.Geophys. Res.* **2005**, 110, D11210.

35. Petters, M. D.; Carrico, C. M.; Kreidenweis, S. M.; Prenni, A. J.; DeMott, P. J.; Collett Jr., J. L.; Moosmüller, H., Cloud Condensation Nucleation Activity of Biomass Burning Aerosol. *J.Geophys. Res.* **2009**, 114, D22205.

36. Dymarska, M.; Murray, B. J.; Sun, L. M.; Eastwood, M. L.; Knopf, D. A.; Bertram, A. K., Deposition Ice Nucleation on Soot at Temperatures Relevant for the Lower Troposphere. *J.Geophys. Res.* **2006**, 111, D04204.

37. Kanji, Z. A.; Ladino, L. A.; Wex, H.; Boose, Y.; Burkert-Kohn, M.; Cziczo, D. J.; Krämer, M., Overview of Ice Nucleating Particles. *Meteorol. Monogr.* **2017**, 58, 1.1-1.33.

38. Suzanne, J.; Ferry, D.; Popovitcheva, O. B.; Shonija, N. K., Ice Nucleation by Kerosene Soot under Upper Tropospheric Conditions. *Can. J. Phys.* **2003**, 81, 423-429.

39. Tishkova, V.; Demirdjian, B.; Ferry, D.; Johnson, M., Neutron Diffraction Study of Water Freezing on Aircraft Engine Combustor Soot. *Phys. Chem. Chem.Phys.* **2011**, 13, 20729-20735.

40. Mahrt, F.; Marcolli, C.; David, R. O.; Grönquist, P.; Barthazy Meier, E. J.; Lohmann, U.; Kanji, Z. A., Ice Nucleation Abilities of Soot Particles Determined with the Horizontal Ice Nucleation Chamber. *Atmos. Chem. Phys.* **2018**, 18, 13363-13392.

41. Friedman, B.; Kulkarni, G.; Beranek, J.; Zelenyuk, A.; Thornton, J. A.; Cziczo, D. J., Ice Nucleation and Droplet Formation by Bare and Coated Soot Particles. *J.Geophys. Res.* **2011**, 116, D17203.

42. Kulkarni, G., et al., Ice Nucleation Activity of Diesel Soot Particles at Cirrus Relevant Temperature Conditions: Effects of Hydration, Secondary Organics Coating, Soot Morphology, and Coagulation. *Geophys. Res. Lett.* **2016**, 43, 3580-3588.

43. Chou, C.; Kanji, Z. A.; Stetzer, O.; Tritscher, T.; Chirico, R.; Heringa, M. F.; Weingartner, E.; Prévôt, A. S. H.; Baltensperger, U.; Lohmann, U., Effect of Photochemical Ageing on the Ice Nucleation Properties of Diesel and Wood Burning Particles. *Atmos. Chem. Phys.* **2013**, 13, 761-772.

44. Charnawskas, J. C.; Alpert, P.A.; Lambe, A.T., Berkemeier, T.; O'Brien, R.E.; Massoli, P.; Onash, T.B.; Shiraiwa, M.; Moffet, R.C.; Gilles, M.K.; Davidovits, P.; Worsnop, D.R.; Knopf,

D.A., Condensed-Phase Biogenic–Anthropogenic Interactions with Implications for Cold Cloud Formation. *Faraday Discuss.* **2017**, 200, 165-194.

45. Whale, T. F.; Rosillo-Lopez, M.; Murray, B. J.; Salzmann, C. G., Ice Nucleation Properties of Oxidized Carbon Nanomaterials. *J. Phys. Chem. Lett.* **2015**, 6, 3012-3016.

46. Brooks, S. D.; Suter, K.; Olivarez, L., Effects of Chemical Aging on the Ice Nucleation Activity of Soot and Polycyclic Aromatic Hydrocarbon Aerosols. *J. Phys. Chem. A* **2014**, 118, 10036-10047.

47. Umo, N. S.; Wagner, R.; Ullrich, R.; Kiselev, A.; Saathoff, H.; Weidler, P. G.; Cziczo, D. J.; Leisner, T.; Möhler, O., Enhanced Ice Nucleation Activity of Coal Fly Ash Aerosol Particles Initiated by Ice-Filled Pores. *Atmos. Chem. Phys.* **2019**, 19, 8783-8800.

48. Tang, I. N.; Munkelwitz, H. R., Composition and Temperature Dependence of the Deliquescence Properties of Hygroscopic Aerosols. *Atmos. Environ., Part A.* **1993**, 27, 467-473.

49. Koop, T.; Kapilashrami, A.; Molina, L. T.; Molina, M. J., Phase Transitions of Sea-Salt/Water Mixtures at Low Temperatures: Implications for Ozone Chemistry in the Polar Marine Boundary Layer. *J. Geophys. Res.: Atmos.* **2000**, 105, 26393-26402.

50. Wise, M. E.; Baustian, K. J.; Koop, T.; Freedman, M. A.; Jensen, E. J.; Tolbert, M. A., Depositional Ice Nucleation onto Crystalline Hydrated Nacl Particles: A New Mechanism for Ice Formation in the Troposphere. *Atmos. Chem. Phys.* **2012**, 12, 1121-1134.

51. Parent, P.; Laffon, C.; Marhaba, I.; Ferry, D.; Regier, T. Z.; Ortega, I. K.; Chazallon, B.; Carpentier, Y.; Focsa, C., Nanoscale Characterization of Aircraft Soot: A High-Resolution Transmission Electron Microscopy, Raman Spectroscopy, X-Ray Photoelectron and near-Edge X-Ray Absorption Spectroscopy Study. *Carbon* **2016**, 101, 86-100.

52. Campbell, J. M.; Meldrum, F. C.; Christenson, H. K., Is Ice Nucleation from Supercooled Water Insensitive to Surface Roughness? J. *Phys. Chem. C* **2015**, 119, 1164-1169.

53. Ouf, F. X.; Parent, P.; Laffon, C.; Marhaba, I.; Ferry, D.; Marcillaud, B.; Antonsson, E.; Benkoula, S.; Lui, X.-J.; Nicolas, C.; Robert, E.; Panaten, M., Barreda, F.-A.; Sublemontier, O.; Copalle, A.; Yon, J.; Miserque, F.; Mostefaoui, T.; Regier, T. Z.; Mitchell, J.-B.A.; Miron, C., First in-Flight Synchrotron X-Ray Absorption and Photoemission Study of Carbon Soot Nanoparticles. *Sci. Rep.* **2016**, 6, 36495.

54. Ess, M. N.; Ferry, D.; Kireeva, E. D.; Niessner, R.; Ouf, F. X.; Ivleva, N. P., In Situ Raman Microspectroscopic Analysis of Soot Samples with Different Organic Carbon Content: Structural Changes During Heating. *Carbon* **2016**, 105, 572-585.

55. Duca, D.; Irimiea, C.; Faccinetto, A.; Noble, J. A.; Vojkovic, M.; Carpentier, Y.; Ortega, I. K.; Pirim, C.; Focsa, C., On the Benefits of Using Multivariate Analysis in Mass Spectrometric Studies of Combustion-Generated Aerosols. *Faraday Discuss*. **2019**, 218, 115-137.

56. Ngo, L. D.; Duca, D.; Carpentier, Y., Noble, J.A., Ikhenazene, R.; Vojkovic, M.; Irimiea, C.; Ortega, I.K.; Lefevre, G.; Yon, J.; Faccinetto, A.; Therssen, E.; Ziskind, M.; Pirim, C.; Focsa, C., Chemical Discrimination of the Particulate-Bound and Gas Phases of Minicast Exhaust Using a Two-filter Collection Method. *Atmos. Meas. Tech. Discussions* **2019**. DOI: 10.5194/amt-2019-275

57. Focsa, C.; Chazallon, B.; Destombes, J. L., Resonant Desorption of Ice with a Tunable $LiNbO_3$ Optical Parametric Oscillator. *Surf. Sci.* **2003**, 528, 189-195.

58. Focsa, C.; Destombes, J. L., $Na/K(H_2O)_n$ Clusters Produced by Laser Desorption of Na/K Salt Doped Ice. *Chem. Phys. Lett.* **2001**, 347, 390-396.

59. Mihesan, C.; Lebrun, N.; Ziskind, M.; Chazallon, B.; Focsa, C.; Destombes, J. L., IR Laser Resonant Desorption of Formaldehyde–H_2O Ices: Hydrated Cluster Formation and Velocity Distribution. *Surf. Sci.* **2004**, 566-568, 650-658.

60. Mihesan, C.; Ziskind, M.; Therssen, E.; Desgroux, P.; Focsa, C., IR Laser Resonant Desorption of Polycyclic Aromatic Hydrocarbons. *Chem. Phys. Lett*. **2006**, 423, 407-412.

61. Mihesan, C.; Ziskind, M.; Therssen, E.; Desgroux, P.; Focsa, C., Parametric Study of Polycyclic Aromatic Hydrocarbon Laser Desorption. *J. Phys.: Condens. Matter* **2007**, 20, 025221.

62. Butcher, D. J., Vacuum Ultraviolet Radiation for Single-Photoionization Mass Spectrometry: A Review. *Microchem. J.* **1999**, 62, 354-362.

63. Desgroux, P.; Mercier, X.; Thomson, K. A., Study of the Formation of Soot and Its Precursors in Flames Using Optical Diagnostics. *Proc. Combust. Inst.* **2013**, 34, 1713-1738.

64. Faccinetto, A.; Desgroux, P.; Ziskind, M.; Therssen, E.; Focsa, C., High-Sensitivity Detection of Polycyclic Aromatic Hydrocarbons Adsorbed onto Soot Particles Using Laser Desorption/Laser Ionization/Time-of-Flight Mass Spectrometry: An Approach to Studying the Soot Inception Process in Low-Pressure Flames. *Combust. Flame* **2011**, 158, 227-239.

65. Faccinetto, A.; Focsa, C.; Desgroux, P.; Ziskind, M., Progress toward the Quantitative Analysis of Pahs Adsorbed on Soot by Laser Desorption/Laser Ionization/Time-of-Flight Mass Spectrometry. *Environ. Sci. Technol.* **2015**, 49, 10510-10520.

66. Cheng, Y.; Su, H.; Koop, T.; Mikhailov, E.; Pöschl, U., Size Dependence of Phase Transitions in Aerosol Nanoparticles. *Nat. Commun.* **2015**, 6, 5923.

67. Bailey, M.; Hallett, J., Growth Rates and Habits of Ice Crystals between -20 Degrees and -70 Degrees C. *J. Atmos. Sci.* **2004**, 61, 514-544.

68. Bailey, M. P.; Hallett, J., A Comprehensive Habit Diagram for Atmospheric Ice Crystals: Confirmation from the Laboratory, AIRS II, and Other Field Studies. *J. Atmos. Sci.* **2009**, 66, 2888-2899.

69. Ullrich, R.; Hoose, C.; Möhler, O.; Niemand, M.; Wagner, R.; Höhler, K.; Hiranuma, N.; Saathoff, H.; Leisner, T., A New Ice Nucleation Active Site Parameterization for Desert Dust and Soot. *J. Atmos. Sci*. **2017**, 74, 699-717.

70. Kanji, Z. A.; Abbatt, J. P. D., Laboratory Studies of Ice Formation Via Deposition Mode Nucleation onto Mineral Dust and N-Hexane Soot Samples. *J. Geophys. Res.: Atmos.* **2006**, 111, D16204.

71. Koop, T.; Luo, B.; Tsias, A.; Peter, T., Water Activity as the Determinant for Homogeneous Ice Nucleation in Aqueous Solutions. *Nature* **2000**, 406, 611-614.

72. Kanji, Z. A.; Florea, O.; Abbatt, J. P. D., Ice Formation Via Deposition Nucleation on Mineral Dust and Organics: Dependence of Onset Relative Humidity on Total Particulate Surface Area. *Environ. Res. Lett.* **2008**, 3, 025004.

73. Hartmann, S.; Wex, H.; Clauss, T.; Augustin-Bauditz, S.; Niedermeier, D.; Rösch, M.; Stratmann, F., Immersion Freezing of Kaolinite: Scaling with Particle Surface Area. *J. Atmos. Sci.* **2016**, 73, 263-278.

74. Welti, A.; Lüönd, F.; Stetzer, O.; Lohmann, U., Influence of Particle Size on the Ice Nucleating Ability of Mineral Dusts. *Atmos. Chem. Phys.* **2009**, 9, 6705-6715.

75. Freedman, M. A., Potential Sites for Ice Nucleation on Aluminosilicate Clay Minerals and Related Materials. *J. Phys. Chem. Lett*. **2015**, 6, 3850-3858.

76. Vali, G., Interpretation of Freezing Nucleation Experiments: Singular and Stochastic; Sites and Surfaces. *Atmos. Chem. Phys.* **2014**, 14, 5271-5294.

77. Phillips, V. T. J.; DeMott, P. J.; Andronache, C., An Empirical Parameterization of Heterogeneous Ice Nucleation for Multiple Chemical Species of Aerosol. *J. Atmos. Sci.* **2008**, 65, 2757-2783.

78. Niedermeier, D.; Shaw, R. A.; Hartmann, S.; Wex, H.; Clauss, T.; Voigtländer, J.; Stratmann, F., Heterogeneous Ice Nucleation: Exploring the Transition from Stochastic to Singular Freezing Behavior. *Atmos. Chem. Phys.* **2011**, 11, 8767-8775.

79. Monge, M. E.; D'Anna, B.; Mazri, L.; Giroir-Fendler, A.; Ammann, M.; Donaldson, D. J.; George, C., Light Changes the Atmospheric Reactivity of Soot. *Proc. Natl. Acad. Sci. U. S. A.* **2010**, 107, 6605-6609.

80. Kim, J.; Bauer, H.; Dobovičnik, T.; Hitzenberger, R.; Lottin, D.; Ferry, D.; Petzold, A., Assessing Optical Properties and Refractive Index of Combustion Aerosol Particles through Combined Experimental and Modeling Studies. *Aerosol Sci. Technol.* **2015**, 49, 340-350.

81. Mamakos, A.; Khalek, I.; Giannelli, R.; Spears, M., Characterization of Combustion Aerosol Produced by a Mini-Cast and Treated in a Catalytic Stripper. *Aerosol Sci. Technol.* **201**3, 47, 927-936.

82. Moore, R. H.; Ziemba, L. D.; Dutcher, D.; Beyersdorf, A. J.; Chan, K.; Crumeyrolle, S.; Raymond, T. M.; Thornhill, K. L.; Winstead, E. L.; Anderson, B. E., Mapping the Operation of the Miniature Combustion Aerosol Standard (Mini-CAST) Soot Generator. *Aerosol Sci. Technol.* **2014**, 48, 467-479.

83. Yon, J.; Bescond, A.; Ouf, F. X., A Simple Semi-Empirical Model for Effective Density Measurements of Fractal Aggregates. *J. Aerosol. Sci.* **2015**, 87, 28-37.

84. Bescond, A.; Yon, J.; Ouf, F. X.; Ferry, D.; Delhaye, D.; Gaffié, D.; Coppalle, A.; Rozé, C., Automated Determination of Aggregate Primary Particle Size Distribution by Tem Image Analysis: Application to Soot. *Aerosol Sci. Technol.* **2014**, 48, 831-841.

85. Häusler, T.; Gebhardt, P.; Iglesias, D.; Rameshan, C.; Marchesan, S.; Eder, D.; Grothe, H., Ice Nucleation Activity of Graphene and Graphene Oxides. *J. Phys. Chem. C* **2018**, 122, 8182-8190.

86. Xue, H.; Lu, Y.; Geng, H.; Dong, B.; Wu, S.; Fan, Q.; Zhang, Z.; Li, X.; Zhou, X.; Wang, J., Hydroxyl Groups on the Graphene Surfaces Facilitate Ice Nucleation. *J. Phys. Chem. Lett.* **2019**, 10, 2458-2462.

87. Sedov, I. A.; Solomonov, B. N., Relation between the Characteristic Molecular Volume and Hydrophobicity of Nonpolar Molecules. *J. Chem. Thermodyn*. **2010**, 42, 1126-1130.

88. Lu, G.-N.; Dang, Z.; Tao, X.-Q.; Yang, C.; Yi, X.-Y., Estimation of Water Solubility of Polycyclic Aromatic Hydrocarbons Using Quantum Chemical Descriptors and Partial Least Squares. *QSAR Comb. Sci.* **2008**, 27, 618-626.

89. Cox, S. J.; Kathmann, S. M.; Slater, B.; Michaelides, A., Molecular Simulations of Heterogeneous Ice Nucleation. II. Peeling Back the Layers. *J. Chem. Phys.* **2015**, 142, 184705.

90. Demirdjian, B.; Ferry, D.; Suzanne, J.; Popovicheva, O.B.; Persiantseva, N. M.; Kamazv, A.V.; Shonija, N.K.; Zubareva, N.A., Freezing of Water Adsorbed on Hydrophobic and Activated Soot Particles. *Chem. Phys. Lett*. **2009**, 480, 247-252.

91. Mueller, L., Jakobi, G.; Orasche, J.; Karg, E.; Sklorz, M.; Abbaszade, G.; Weggler, B.; Jing, L.; Schnelle-Kreis, J.; Zimmermann, R., Online Determination of Polycyclic Aromatic Hydrocarbon Formation from a Flame Soot Generator. *Anal. Bioanal. Chem*. **2015**, 407, 5911-5922.

92. Fitzner, M.; Sosso, G. C.; Cox, S. J.; Michaelides, A., The Many Faces of Heterogeneous Ice Nucleation: Interplay between Surface Morphology and Hydrophobicity. *J. Am. Chem. Soc.* **2015**, 137, 13658-13669.

93. Hedges, L. O.; Whitelam, S., Selective Nucleation in Porous Media. *Soft Matter* 2013, 9, 9763-9766.

94. Holbrough, J. L.; Campbell, J. M.; Meldrum, F. C.; Christenson, H. K., Topographical Control of Crystal Nucleation. *Cryst. Growth Des.* **2012**, 12, 750-755.

95. Lupi, L.; Hudait, A.; Molinero, V., Heterogeneous Nucleation of Ice on Carbon Surfaces. *J. Am. Chem. Soc.* **2014**, 136, 3156-3164.

96. Marcolli, C., Deposition Nucleation Viewed as Homogeneous or Immersion Freezing in Pores and Cavities. *Atmos. Chem. Phys.* **2014**, 14, 2071-2104.

97. Page, A. J.; Sear, R. P., Heterogeneous Nucleation in and out of Pores. *Phys. Rev. Lett*. **2006**, 97, 065701.

98. Page, A. J.; Sear, R. P., Crystallization Controlled by the Geometry of a Surface. *J. Am. Chem. Soc.* **2009**, 131, 17550-17551.

99. Wagner, R.; Kiselev, A.; Möhler, O.; Saathoff, H.; Steinke, I., Pre-Activation of Ice-Nucleating Particles by the Pore Condensation and Freezing Mechanism. *Atmos. Chem. Phys.* **2016**, 16, 2025-2042.

100. David, R. O.; Marcolli, C.; Fahrni, J.; Qiu, Y.; Perez Sirkin, Y. A.; Molinero, V.; Mahrt, F.; Brühwiler, D.; Lohmann, U.; Kanji, Z. A., Pore Condensation and Freezing Is Responsible for Ice Formation Below Water Saturation for Porous Particles. *Proc. Natl. Acad. Sci. U. S. A.* **2019**, 116, 8184-8189.

101. Dijkstra, T. A.; Smalley, I. J.; Rogers, C. D. F., Particle Packing in Loess Deposits and the Problem of Structure Collapse and Hydroconsolidation. *Eng. Geol.* **1995**, 40, 49-64.

102. Dixkens, J.; Fissan, H., Development of an Electrostatic Precipitator for Off-Line Particle Analysis. *Aerosol Sci. Technol.* **1999**, 30, 438-453.

103. Thomas, D.; Ouf, F. X.; Gensdarmes, F.; Bourrous, S.; Bouilloux, L., Pressure Drop Model for Nanostructured Deposits. *Sep. Purif. Technol.* 2014, 138, 144-152.

104. Andersson, P. U.; Suter, M. T.; Marković, N.; Pettersson, J. B. C., Water Condensation on Graphite Studied by Elastic Helium Scattering and Molecular Dynamics Simulations. *J. Phys. Chem. C* **2007**, 111, 15258-15266.

105. Kong, X.; Andersson, P. U.; Thomson, E. S.; Pettersson, J. B. C., Ice Formation Via Deposition Mode Nucleation on Bare and Alcohol-Covered Graphite Surfaces. *J. Phys. Chem. C* **2012**, 116, 8964-8974.

106. Campbell, J. M.; Meldrum, F. C.; Christenson, H. K., Characterization of Preferred Crystal Nucleation Sites on Mica Surfaces. *Cryst. Growth Des.* **2013**, 13, 1915-1925.

107. Eckmann, A.; Felten, A.; Mishchenko, A.; Britnell, L.; Krupke, R.; Novoselov, K. S.; Casiraghi, C., Probing the Nature of Defects in Graphene by Raman Spectroscopy. *Nano Lett.* **2012**, 12, 3925-3930.

Supporting Information

Introduction

The SI provides details (2 Texts, 5 Figures, and 2 Tables) on how our samples were produced (Table S1), provides further information on the optical technique we developed to represent our sample surface areas (Figures S1-S5), shows how was calculated the growth rate of a columnar crystal (Figure S5), and how the porosity of our samples has been assessed using their hydraulic diameter as a proxy (Table S2).

Text S1.

Supporting information for saturation ratio with respect to ice (Si) determination. S_i is defined as the ratio of the partial vapor pressure (e) at a given frost point (FP) temperature when nucleation is observed to the saturation vapor pressure above ice expected at this nucleation onset temperature ($e_{sat,i}$); data are derived from the cryo-hygrometer and the calibrated sample temperature. In the humidity and temperature range of interest in this study, our experimental vapor pressure is in line with that of hexagonal ice calculated in Murphy and Koop (2005).[S1]

As T_{sample} is critical in the S_i calculation, it is necessary to accurately assess the substrate temperature, as particles and films are not directly deposited onto the heat exchanger block but rather onto a 185 µm-thick silicon wafer. The silicon wafer temperature was evaluated monitoring phase changes of 1-µL pure solution droplets. Freezing and melting phases of 4 undecane and nonanol solution droplets have been subsequently optically monitored using a temperature ramp of 0.2 °C. The melting temperatures were recorded twice for each chemical and then compared to their known temperature (-25.6 °C and -5 °C for undecane and nonanol, respectively). A difference of 0.1 °C was observed over this temperature range.

In addition, as soot is collected onto such silicon wafers, it is necessary to evaluate whether the soot top layer temperature is the same as that of the silicon substrate, as it is where the main interaction between

water vapor and soot occurs. Consequently, a one-dimensional thermodynamics equation (Eq. S1) was used to approximately estimate the temperature drop from the cold substrate to the soot surface:

$$T_{soot} = (T_{Si} - T_{air}) \times \left[\cosh\frac{l}{x_0} - \frac{\tanh\frac{l}{x_0} + \frac{hx_0}{K}}{1 + \frac{hx_0}{K}\tanh\frac{l}{x_0}} \sinh\frac{l}{x_0} \right] + T_{air} \qquad \text{with} \qquad x_0 = \sqrt{\frac{Ka}{2h}} \qquad \textbf{Eq. (S1)}$$

where T_{soot} is the soot top layer temperature, T_{Si} is the silicon substrate temperature (here 228 K), T_{air} is the fluid temperature (300 K) surrounding the soot sample, l is the soot thickness (30.10^{-6} m), x_0 is a length parameter ($7.8.10^{-3}$ m) whose equation is shown, h is the heat transfer coefficient of a low speed flow of air over the soot surface (10 $W.m^{-2}K^{-1}$), a is the radius of the cylindrical soot sample (11.10^{-3} m), and K is the thermal conductivity of a standard soot material (0.11 $W.m^{-1}.K^{-1}$). [S 2- S 3]

In this simplified model, T_{soot} is assumed to solely be a function of the distance between the cold substrate and the uppermost soot layer exposed to the warm airflow (i.e., function of soot thickness). For an upper thickness limit estimate of 30 µm, the calculation gives a T_{soot} of -44.95°C for a T_{Si} of -45°C. Therefore, the soot surface is considered to be at the same temperature as the silicon substrate. Note that the soot thickness upper limit was estimated using Fourier transform infrared measurements in which the fringing effect was observed. [S4] The optical method developed for surface analysis and described hereafter further confirms the order of magnitude for our thickness estimate.

The contribution to the total error on S_{ice} from the errors on the FP (±0.15°C) and T_{sample} (± 2%) are determined using the calculus-based approximation for independent multi-variable functions by adding the components from each variable in quadrature and thus varies of about 3.5% at the coldest temperature.

Text S2.

Supporting information for soot porosity determination. For all material/gas-vapor interactions, structure of the matrix is crucial for understanding these complex phenomena. In the present section we

propose a simple semi-empirical approach for determining the porosity and the pore size at the soot deposit surface.

Soot particles have been deposited using an electrostatic precipitator (Nanometer Aerosol Sampler 3089 from TSI ©) directly on analysis substrates. Considering applied tension and flow-rate (respectively -10 kV and 1.5 L/min), the deposition velocity (V_{dep}) within the NAS has been computed, for each soot samples (CAST-1 and 3) from their electrical mobility diameter (D_p) and according to Dixkens et al. (1999) S5

Using these deposition velocities, the porosity (Φ) of the deposit has been determined by computing the Peclet number (Pe) of soot aggregates and according to the semi-empirical relationship introduced by Thomas et al. (2014):

$$\mathrm{Pe} = \frac{V_{dep} d_p}{D}; \quad \textbf{Eq. (S2)} \qquad \phi = \frac{1+0.44\,\mathrm{Pe}}{1.019+0.46\,\mathrm{Pe}} \quad \textbf{Eq. (S3)}$$

where D is the particle diffusion coefficient (calculated with D_p according to the Stokes–Einstein equation).

Finally and according to Dijkstra et al. (1995), this porosity is used to compute the hydraulic diameter of the soot deposit, which is commonly assumed to be a satisfactory parameter for correlation of single-phase flow in porous media:

$$D_h = \frac{\Phi D_p}{3(1-\Phi)} \quad \textbf{Eq. (S4)}$$

Results obtained from all these assumptions are summarized in table S2.

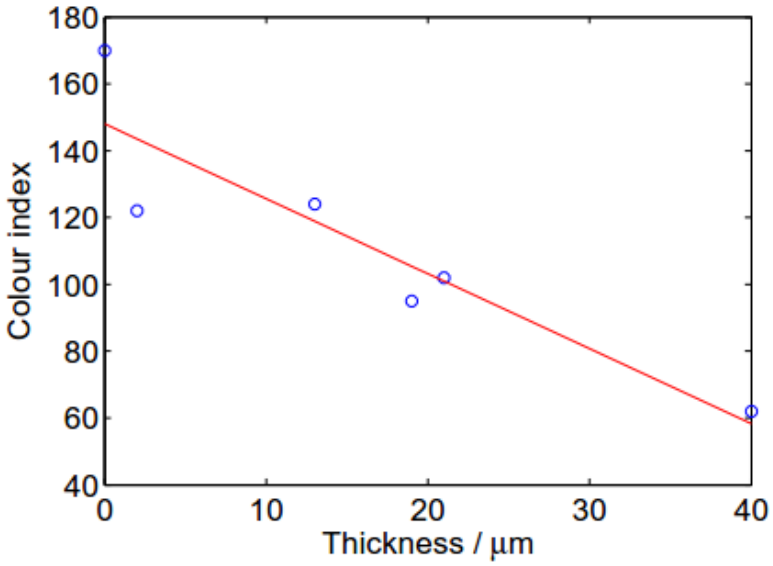

Figure S1. Calibration of color index with soot thickness. Experimental data points are plotted as blue circles, and a linear fit to these data is plotted in red.

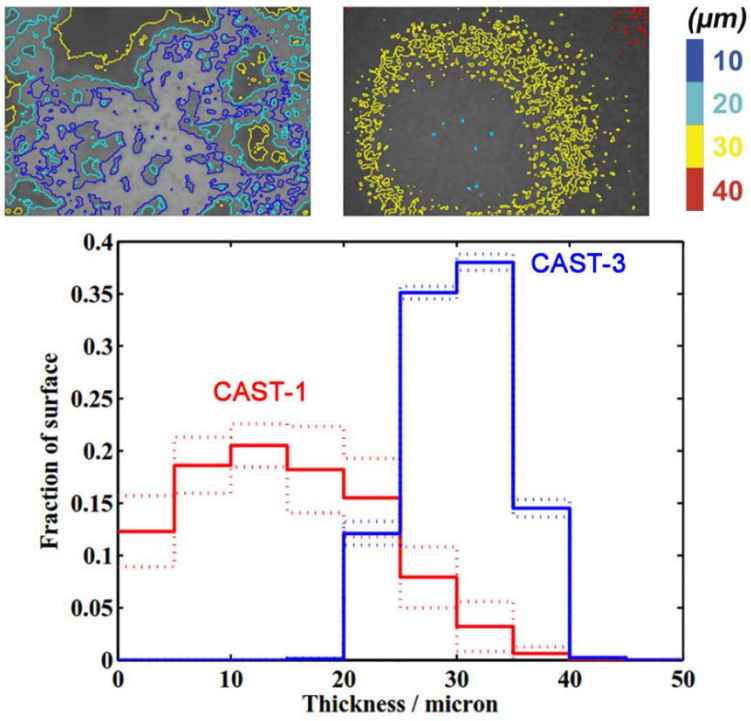

Figure S2. Numerical analysis of the thickness of soot on the CAST-1 and CAST-3 samples. The derived soot surfaces for each image were divided into bins of five microns thickness. The upper panels of Figure S2 show the central images (X0,Y0) for the CAST-1-type (left) and CAST-3 -type (right) samples with contour lines at the following soot thicknesses: 10 (dark blue), 20 (light blue), 30 (yellow), and 40 (red)

μm. Bottom panel: the fraction of the sample area as a function of thickness for CAST-1 and CAST-3 soot samples. The dotted lines represent the 3 σ confidence levels. The CAST-1-type soot has both a larger thickness distribution and a wider image-to-image variation (i.e. higher standard deviation) than the CAST-3-type soot, which has a narrow, well-defined distribution centered around ≈30 microns.

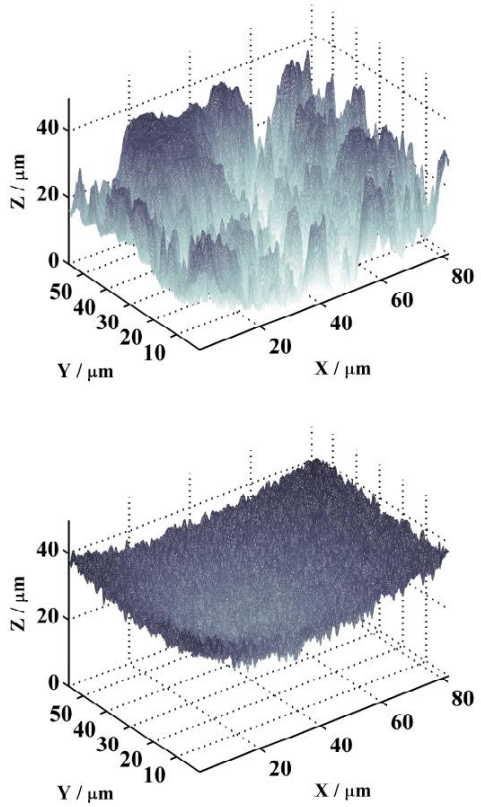

Figure S3. Soot surface representations derived for CAST-1 (upper panel) and CAST-3 (lower panel) soot samples at (X_0, Y_0).

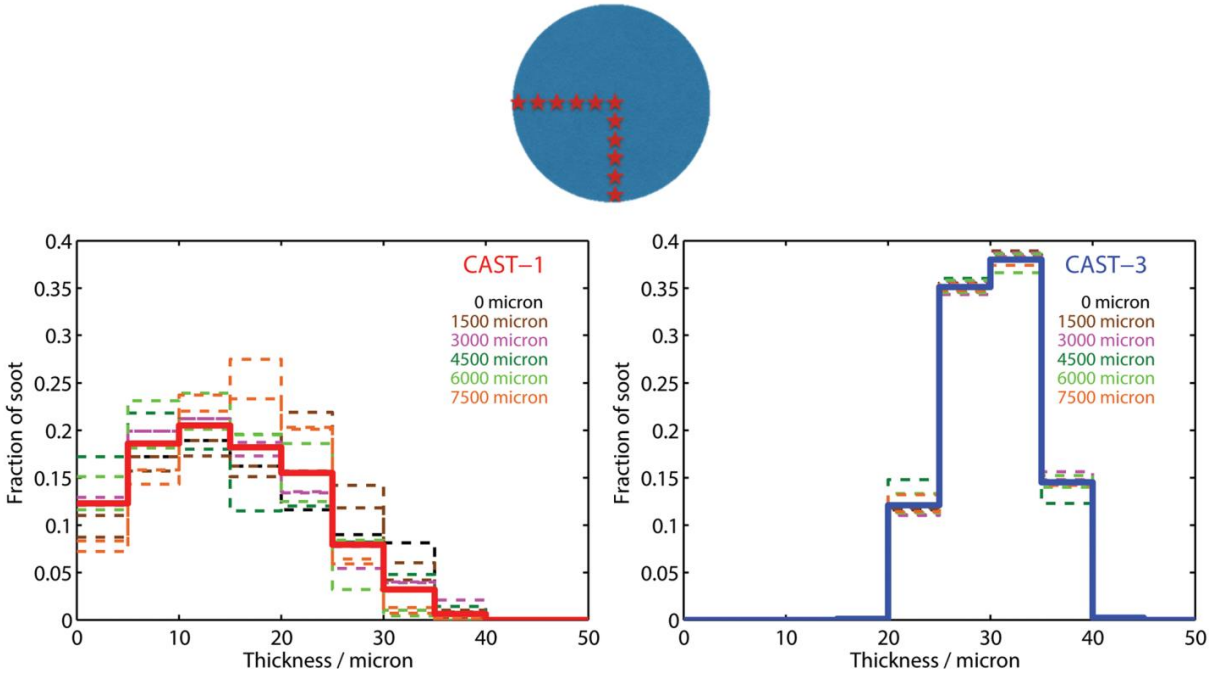

Figure S4. Derived thickness distributions (0→7500 μm) as a function of distance from the sample center (red stars = positions) for CAST-1 (left) and CAST-3 (right). The position-dependent (see red stars represented schematically at the top) thickness distributions are plotted with dashed lines, while the overall sample average is plotted in a thick, solid line.

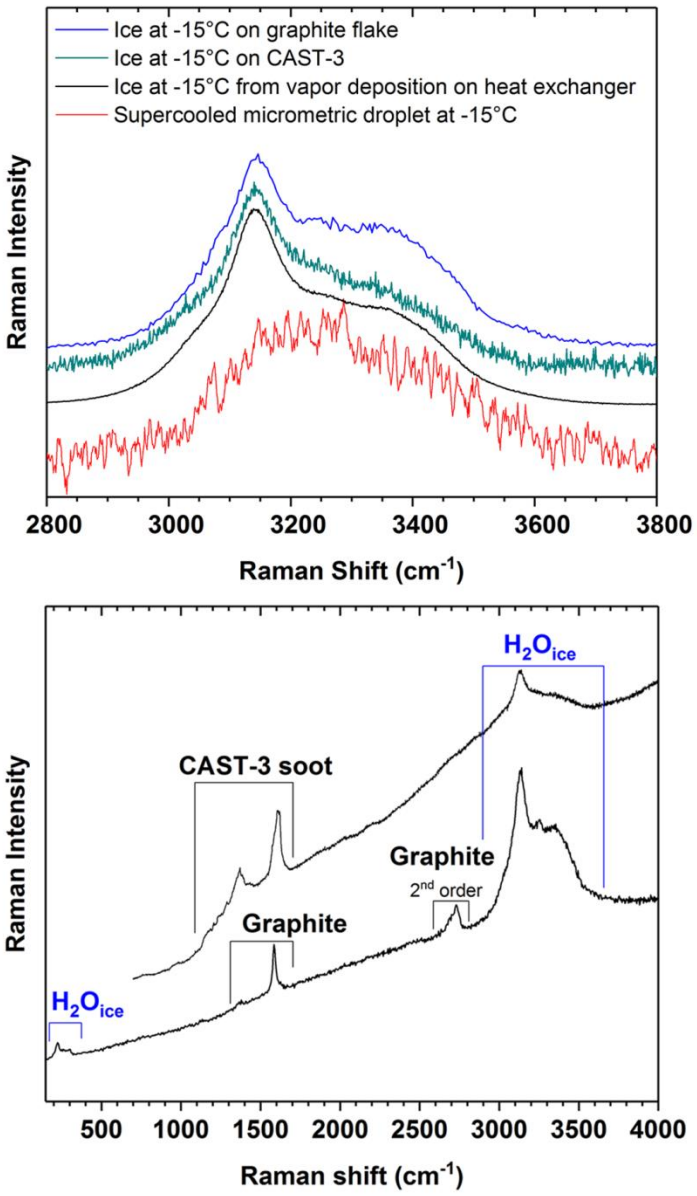

Figure S5. Nucleation monitoring via micro-Raman. Top) Raman spectra of a supercooled droplet, an ice crystal growing on CAST-3 or graphite, and that of an ice crystal formed from vapor deposition onto the heat exchanger. Nucleus growth and spectra were all acquired at -15°C in the spectral region corresponding to the O-H stretching vibration bands. Bottom) Extended Raman spectra of ice growing on either CAST-3 soot particles or graphite flakes at -45°C.

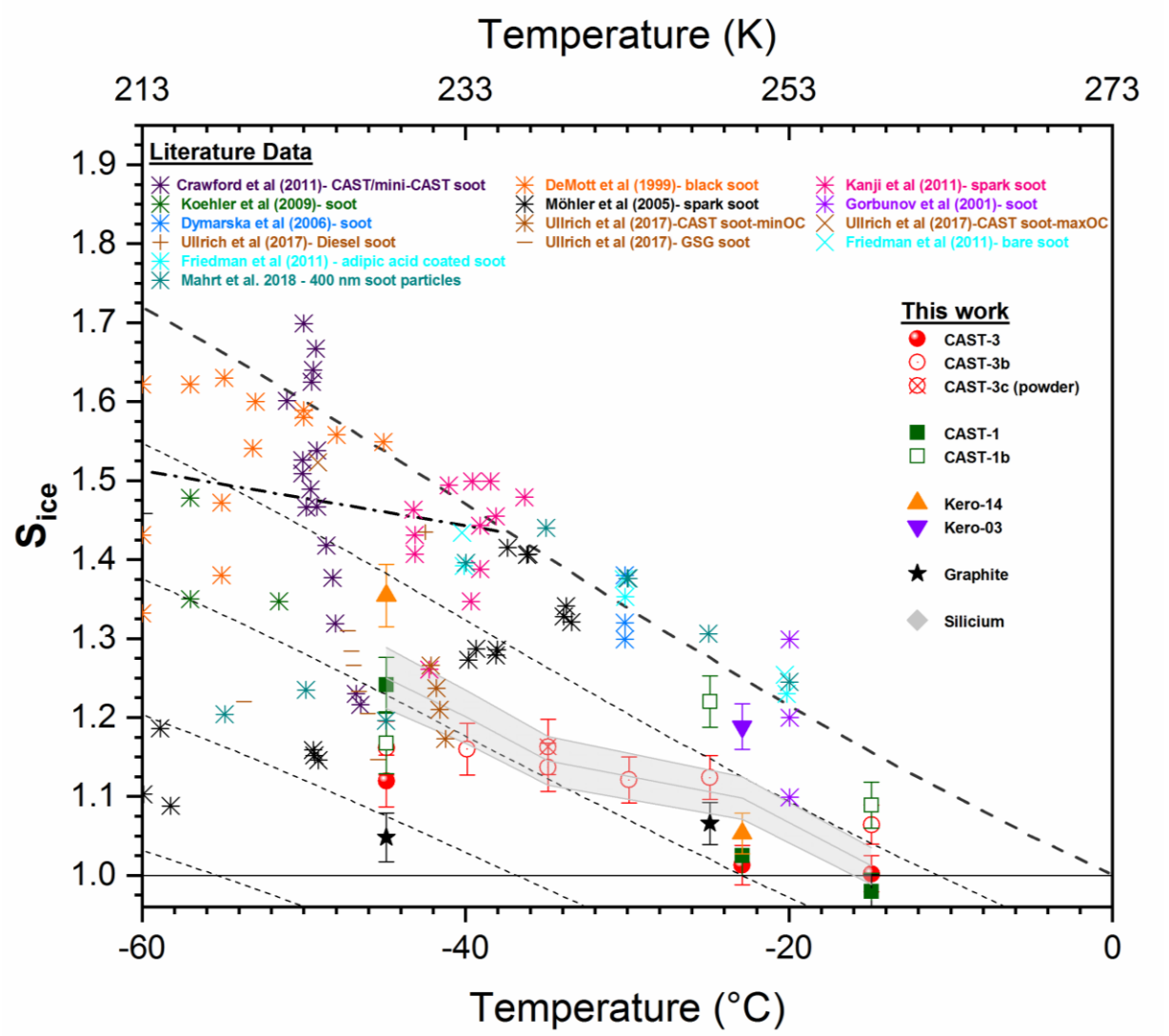

Figure S6. a) Ice nucleation onset temperatures (first nucleus detected) and corresponding saturation ratios with respect to ice for bare silicon and carbon-bearing samples. ● CAST-3, ○ CAST-3b, ⊗ CAST-3c, ■ CAST-1, □ CAST-1b, ▼ Kero-03, ▲ Kero-14, ★ Graphite Flakes. The light grey area shows the ice nucleation onset temperatures obtained for a bare silicon wafer. The horizontal solid black line represents the ice saturation ratio at ice saturation (S_{ice} =1). The bold diagonal dashed line represents the ice saturation ratio at liquid water saturation, and additional relative humidity (RH) ratios with respect to water have been indicated for ease of reading. The dotted-dashed isoline corresponds to the homogeneous freezing of a 200 nm solution droplet.[22, 71] Results obtained in this work are compared with literature data for which complete references are indicated at the end of the SI.

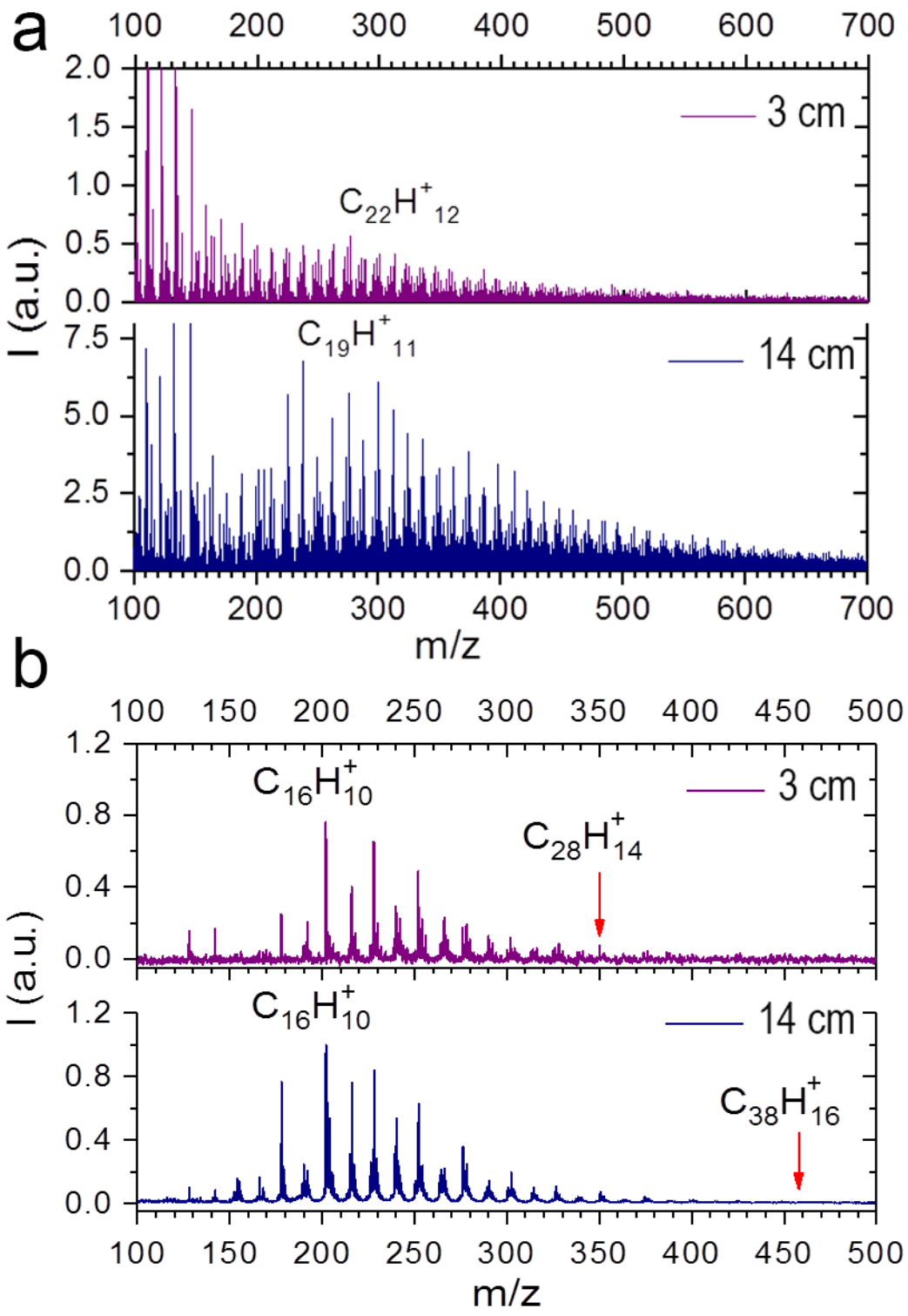

Figure S7. a) SIMS and b) L2MS spectra of kerosene Jet A1 soot samples produced with a McKenna burner and collected on silicon wafers at 3 and 14 cm above the burner.

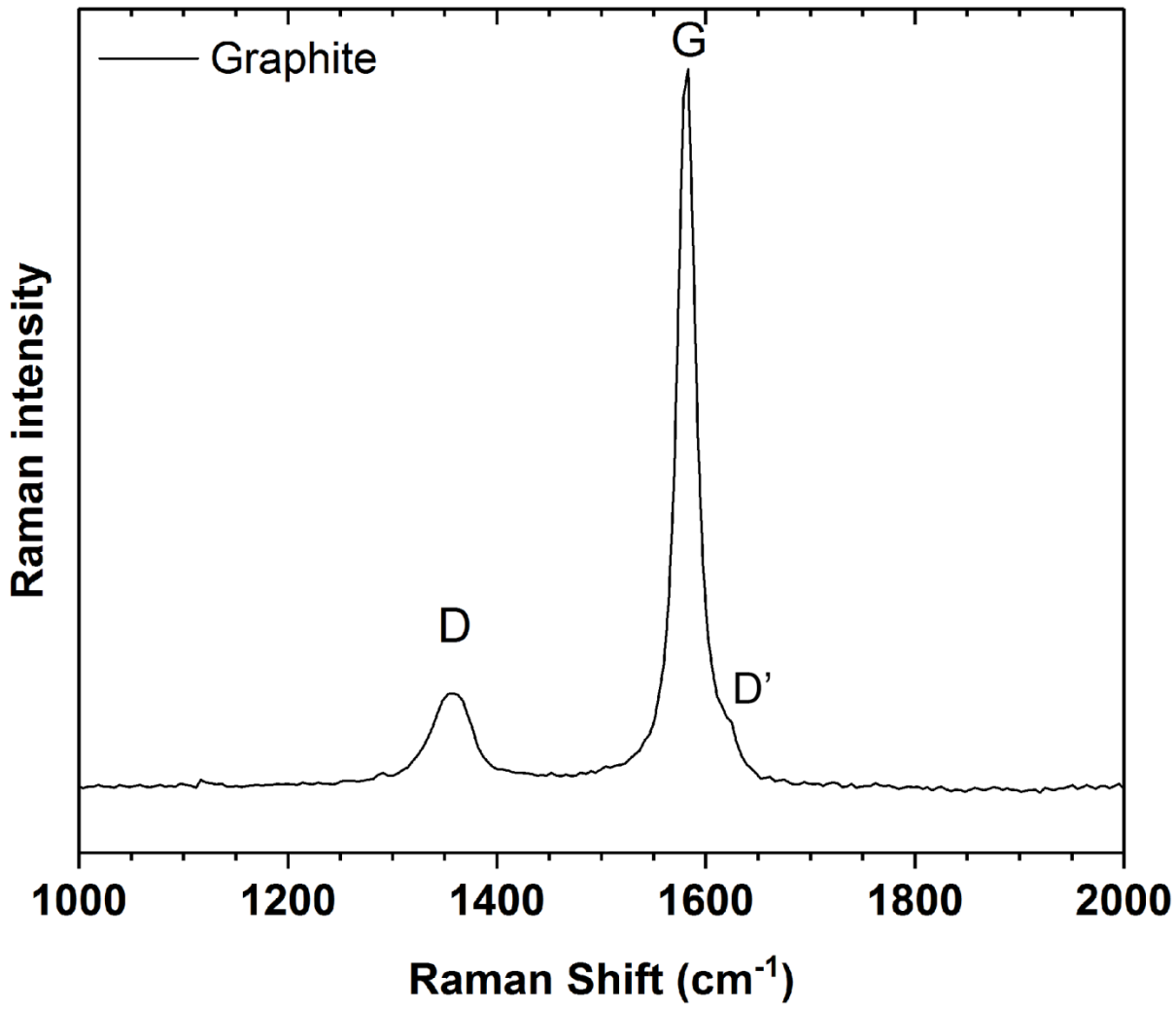

Figure S8. First order Raman spectrum of a graphite flake (excitation wavelength 514.5 nm).

Table S1. miniCAST set points showing the fuel, quench, air oxidation, and dilution gases and flows used to generate soot samples 3, 3b 3c, and 1 and 1b. The organic carbon to total carbon ratio (OC/TC) indicated is from Bescond et al. [S6] Collection time and the aspect of the particles once deposited onto the substrate are also indicated.

Samples	Gas type and Flow (NmL/min)	Fuel	Mixing	Oxidation	Dilution	Quench	OC/TC (%)	Collect. time (min)	Particles deposited as
		C_3H_8	N_2	Air	Air	N_2			
CAST-3		60	0	1000	20	7	87.0	5	granular film
CAST-3b		60	0	1000	20	7	87.0	10	granular film
CAST-3c		60	0	1000	20	7	87.0	N/A	powder
CAST-1		60	0	1500	20	7	4.0	5	fibrous islands
CAST-1b		60	0	1500	20	7	4.0	10	fibrous clumps

Table S2. Results obtained from assumptions in Text S2.

CAST Set Points	Electrical mobility Diameter D_p (nm)	Deposition velocity (cm/s) [S5]	Porosity from and defined as in ref [S7]	Hydraulic Diameter D_h (nm) [S8]
CAST-1	115	0.01	98.1 %	2004 nm
CAST-3	52	3.64	97.4 %	662 nm

References

S-1. Murphy, D. M.; Koop, T., Review of the Vapour Pressures of Ice and Supercooled Water for Atmospheric Applications. **2005**, *131*, 1539-1565.

S-2. Hewitt, G.; Shires, G.; Polezhaev, Y.; Devahastin, S. J. D. T., International Encyclopedia of Heat and Mass Transfer. **1998**, *16*, 1521-1522.

S-3. Haralampous, O.; Koltsakis, G. C., Intra-Layer Temperature Gradients During Regeneration of Diesel Particulate Filters. *Chemical Engineering Science* **2002**, *57*, 2345-2355.

S-4. Griffiths, P. R.; De Haseth, J. A., *Fourier Transform Infrared Spectrometry*; John Wiley & Sons, 2007; Vol. 171.

S-5. Dixkens, J.; Fissan, H., Development of an Electrostatic Precipitator for Off-Line Particle Analysis. *Aerosol Science & Technology* **1999**, *30*, 438-453.

S-6. Bescond, A.; Yon, J.; Ouf, F. X.; Ferry, D.; Delhaye, D.; Gaffié, D.; Coppalle, A.; Rozé, C., Automated Determination of Aggregate Primary Particle Size Distribution by Tem Image Analysis: Application to Soot. *Aerosol Science and Technology* **2014**, *48*, 831-841.

S-7. Thomas, D.; Ouf, F. X.; Gensdarmes, F.; Bourrous, S.; Bouilloux, L., Pressure Drop Model for Nanostructured Deposits. *Separation and Purification Technology* **2014**, *138*, 144-152.

S-8. Dijkstra, T.; Smalley, I.; Rogers, C., Particle Packing in Loess Deposits and the Problem of Structure Collapse and Hydroconsolidation. *Engineering Geology* **1995**, *40*, 49-64.

S-9. Crawford, I., et al., Studies of Propane Flame Soot Acting as Heterogeneous Ice Nuclei in Conjunction with Single Particle Soot Photometer Measurements. Atmospheric Chemistry and Physics 2011, 11, 9549-9561.

S-10. Dymarska, M.; Murray, B. J.; Sun, L. M.; Eastwood, M. L.; Knopf, D. A.; Bertram, A. K., Deposition Ice Nucleation on Soot at Temperatures Relevant for the Lower Troposphere. Journal of Geophysical Research 2006, 111, 9.

S-11. Koehler, K. A.; DeMott, P. J.; Kreidenweis, S. M.; Popovicheva, O. B.; Petters, M. D.; Carrico, C. M.; Kireeva, E. D.; Khokhlova, T. D.; Shonija, N. K., Cloud Condensation Nuclei and Ice Nucleation Activity of Hydrophobic and Hydrophilic Soot Particles. Physical Chemistry Chemical Physics 2009, 11, 7906-7920.

S-12. Friedman, B.; Kulkarni, G.; Beranek, J.; Zelenyuk, A.; Thornton, J. A.; Cziczo, D. J., Ice Nucleation and Droplet Formation by Bare and Coated Soot Particles. Journal of Geophysical Research 2011, 116, 11.

S-13. Ullrich, R.; Hoose, C.; Möhler, O.; Niemand, M.; Wagner, R.; Höhler, K.; Hiranuma, N.; Saathoff, H.; Leisner, T., A New Ice Nucleation Active Site Parameterization for Desert Dust and Soot. J. Atmos. Sci. 2017, 74, 699-717.

S-14. DeMott, P. J.; Chen, Y.; Kreidenweis, S. M.; Rogers, D. C.; Sherman, D. E., Ice Formation by Black Carbon Particles. Geophys. Res. Lett. 1999, 26, 2429-2432.

S-15. Kanji, Z. A.; DeMott, P. J.; Mohler, O.; Abbatt, J. P. D., Results from the University of Toronto Continuous Flow Diffusion Chamber at Icis 2007: Instrument Intercomparison and Ice Onsets for Different Aerosol Types. Atmospheric Chemistry and Physics 2011, 11, 31-41.

S-16. Gorbunov, B.; Baklanov, A.; Kakutkina, N.; Windsor, H. L.; Toumi, R., Ice Nucleation on Soot Particles. J. Aerosol. Sci. 2001, 32, 199-215.

S-17. Möhler, O.; Linke, C.; Saathoff, H.; Schnaiter, M.; Wagner, R.; Mangold, A.; Krämer, M.; Schurath, U., Ice Nucleation on Flame Soot Aerosol of Different Organic Carbon Content. Meteorologische Zeitschrift 2005, 14, 477-484.